NASA CONTRACTOR REPORT

NASA CR-321

A FLIGHT AND WIND TUNNEL INVESTIGATION OF THE EFFECT OF ANGLE-OF-ATTACK RATE ON MAXIMUM LIFT COEFFICIENT

by Fox Conner, Craig Willey, and William Twomey

Prepared under Contract No. NAS 4-471 *by*
LOCKHEED-CALIFORNIA COMPANY
Burbank, Calif.
for

NATIONAL AERONAUTICS AND SPACE ADMINISTRATION • WASHINGTON, D. C. • OCTOBER 1965

NASA CR-321

A FLIGHT AND WIND TUNNEL INVESTIGATION OF THE EFFECT OF ANGLE-OF-ATTACK RATE ON MAXIMUM LIFT COEFFICIENT

By Fox Conner, Craig Willey, and William Twomey

Prepared under Contract No. NAS 4-471 by
LOCKHEED-CALIFORNIA COMPANY
Burbank, Calif.

for

NATIONAL AERONAUTICS AND SPACE ADMINISTRATION

For sale by the Clearinghouse for Federal Scientific and Technical Information
Springfield, Virginia 22151 – Price $3.00

TABLE OF CONTENTS

LIST OF FIGURES

A FLIGHT AND WIND TUNNEL INVESTIGATION OF THE EFFECT OF ANGLE-OF-ATTACK RATE ON MAXIMUM LIFT COEFFICIENT

By Fox Conner, Craig Willey and William Twomey

Lockheed-California Company

SUMMARY

The effect of angle-of-attack rate on maximum lift at stall was investigated for a related series of six half-wing models in a blowdown wind tunnel as well as for a single-engine, jet-propelled airplane. Mach numbers from 0.25 to 0.75, Reynolds numbers from 1.4 to 21 x 10^6, thickness ratios of 9, 13 and 16%, sweep angles of 0 and 35 degrees, aspect ratios of 3 and 6 and cambers corresponding to ideal lift coefficients of 0 and 0.2 were tested. All wings were composed of 65_1-XXX (a = .5) airfoil sections.

The increase in the maximum lift with angle-of-attack rate was small and, in general, linear. There were no clear indications of a limit for the maximum lift obtainable. Of the parameters tested, thickness, camber and sweep had the greatest effect. The effect of angle-of-attack rate on maximum lift was increased as camber of thickness decreased, or sweep increased.

The flight test results correlated with the trends derived from the wind tunnel tests.

INTRODUCTION

The stalling characteristics of a wing are determined by a number of factors including free stream turbulence, wing profile and planform, and Mach and Reynolds numbers. One of the least understood factors is the effect of an angle-of-attack rate which is present during dynamic flight conditions such as pullups and which cannot be ignored in the design of an aircraft. A program to explore the effect of angle-of-attack rate was undertaken during the 1940's and early 1950's by the National Advisory Committee for Aeronautics (now the National Aeronautics and Space Administration). Reference 1 discusses wind tunnel tests of a 1/20 scale partial reproduction of a conventional single-engine aircraft with an elliptical wing of modified NASA 230-series section. The results of flight investigations with propeller-driven, single-engine, fighter-type aircrafts are presented in References 2 and 3.

Aircraft design continues to grow more and more sophisticated with the years and the need has arisen for research which would extend the earlier experiments. Specifically, there was a need to define the effect of an angle-of-attack rate on maximum lift coefficient for a greater range of Mach and Reynolds numbers and for a variety of wing sections and planforms. Only tests

and empirical analysis could provide the answer as boundary layer and potential flow theory was found to be lacking. Even qualitative guides are difficult to establish from the theory, and quantitatively the problem is hopeless unless greatly improved mathematical tools are made available. The basic difficulty lies with boundary layer theory. It is conceptually feasible by relaxation methods, as discussed in Reference 4, to obtain theoretical solutions for combinations of sub- and supersonic flows although a large amount of computing is required. Boundary layer theory for non-steady flows is extremely difficult and poorly developed even for laminar boundary layers. Add to this the difficulties of calculating the point of instability and the point of transition for a laminar boundary layer changing to a turbulent boundary layer and the problem is compounded. Knowledge of whether the boundary layer is laminar or turbulent is necessary for calculating the separation point for the pressure distribution imposed by the potential flow solution. Still another complication arises. If a separation "bubble" exists, then consideration must be made for a free boundary in the potential flow solution. Finally, it may not be possible even to separate the boundary layer from the potential flow solution if small shocks exist close to the section contour.

In answer to the need for additional research, the Lockheed-California Company conducted wind tunnel tests on six half-wing models and flight tests on a jet-propelled, single-engine aircraft under contract NAS4-471 with the National Aeronautics and Space Administration. The six models were derived from NASA 65_1-XXX (a = .5) sections and varied in thickness, camber, aspect ratio and sweepback. One of the models closely represented the wing of the test aircraft.

SYMBOLS

a_x	longitudinal acceleration
a_z	normal acceleration
A	aspect ratio
$\bar{c}$	mean aerodynamic chord
C_L	coefficient of lift
$C_{L_{max}}$	maximum lift coefficient
M	Mach number
R	radius
RN	Reynolds number
t	time
$t/\bar{c}$	thickness ratio
V	true airspeed
α_b	true boom angle-of-attack
α_f	boom angle-of-attack corrected for upwash
α_i	indicated angle-of-attack
$\alpha_{3/4\ \bar{c}}$	angle-of-attack at the wing three-quarter chord point
$\dot{\alpha}$	angle-of-attack rate
Λ	sweep angle
θ	pitch attitude

WIND TUNNEL TESTS

Description of Models

The test articles were six half-span wings which were tested on a floor mounted support system in a 4 ft by 4 ft blowdown wind tunnel. All models had a taper ratio of one and zero geometric twist. Other section and planform characteristics of the models are given below:

Model	Aspect ratio	Sweepback angle, deg	Wing section	Planform area, ft^2	Chord length, ft
W-1	6	0	65_1-209(a = .5)	1/3	1/3
W-2	6	0	65_1-213(a = .5)	1/3	1/3
W-3	6	0	65_1-216(a = .5)	1/3	1/3
W-4	3	0	65_1-213(a = .5)	2/3	2/3
W-5	6	35	65_1-213(a = .5)	1/3	1/3
W-6	6	0	65_1-013	1/3	1/3

Photographs of models W-2 and W-5 installed in the tunnel ready for testing are presented in Figures 1 and 2.

Description of Test Apparatus

The special model support system consisted of a hydraulically-operated rotating disc suspended on a force measuring balance. The disc was positioned three inches off the tunnel floor with the model mounted vertically on the disc. The system permitted a model angle-of-attack range from -5 to +70 degrees. The acceleration to and the deceleration from the programmed angle-of-attack rate was rapid and resulted in the angular velocity being constant from approximately +10 to +40 degrees. A simulated fuselage faired the model disc with the tunnel floor and smoothly directed the tunnel floor boundary layer away from the model.

A constant angle-of-attack rate was obtained through the use of a servo system operating the hydraulic drive system. The drive system consisted of a hydraulic cylinder powered by a 3000 psi pressure source which rotated the disc through a cam device. A hydraulic damper was included in the system to aid in decelerating the model at the end of each run. Control of the servo system was achieved by electronically regulating a hydraulic control valve with an analog computer.

This system provided controlled angular velocities up to 1200 deg/sec. A block diagram of the system is given in Figure 3. In order to prevent excessive quantities of extraneous data, a switch was provided which limited the data acquisition to the part of the run where the angular velocities were constant.

Instrumentation

The wind tunnel test conditions were obtained from a static pressure measurement in the test section plus air temperature and total pressure measurement in the "stilling chamber" upstream of the test section. This instrumentation is standard for all tests in the 4 ft by 4 ft blowdown tunnel.

The force measuring unit consisted of two load cells to measure lift. A complete calibration of the unit was performed prior to the tunnel installation and check loadings were performed periodically during the tests. The angle-of-attack was measured with a calibrated, infinite-resolution dual potentiometer attached to the rotating disc. Electrical signals from the force measuring unit and the angle-of-attack potentiometer were transmitted to the data gathering system where the signals were digitized and subsequently recorded on magnetic tape. The lift and angle-of-attack data were sampled at 1160 points per second for the dynamic stalls.

Test Procedure

Static lift data were obtained by rotating each model at 2 deg/sec for various conditions of Mach and Reynolds numbers. Dynamic runs were completed by rotating the models at eight different rates from 200 to 1200 deg/sec at the same Mach and Reynolds number conditions. All dynamic tests were run twice as a check on repeatability. During the runs, inertia tares were obtained occasionally by rotating the model at the desired rate with the tunnel airflow shut off and recording the loads resulting from mass imbalance. Tests were completed at Mach numbers from 0.25 to 0.75 and at Reynolds numbers from 1.4 to 5.6 x 10^6.

Measurement Errors

Based on an analysis of the data, past experience and repeatability, it is estimated that typical values of the errors are:

Mach number	1%
Reynolds number	1.5%
Lift coefficient	2%
Non-dimensional angle-of-attack rate	1%

where the errors are root-mean-square values.

FLIGHT TESTS

Description of Test Airplane

The test aircraft was the Navy Model T-1A; a two-place, single-engine, jet-propelled, navigation trainer. It was powered by a J33-A-24 gas turbine engine. For the test program the tip tanks were removed and replaced with wing tip fairings, the wing leading-edge slats were locked in the fully-retracted position and the stall inducer strips were removed. All holes were filled in order to obtain a "clean" wing comparable to the wind tunnel models. Figure 4 presents a photograph of a T-1A airplane.

Basic airplane data follow:

Test gross weight	11 700 to 12 200 lb
Test center of gravity, wheels up	25% MAC
Wing span	37.5 ft
Fuselage length	36.5 ft

The geometric parameters describing the wing are:

Area	232.8 ft^2
Aspect ratio	6.05
Taper ratio	0.381
Mean aerodynamic chord	6.72 ft
Sweepback of the 50% chord line	0 deg
Dihedral	3.83 deg
Geometric twist	-1.5 deg
Airfoil section	NASA 65_1-213 (a = .5)

Instrumentation

Flight data were gathered from an automatic observer panel and a four-inch recording oscillograph. The automatic observer consisted of the rear cockpit panel with the test instruments installed and a 35mm automatic camera. The panel included a counter to establish the identity of each oscillograph record and a light to establish the length of the record. Correlation between the automatic observer panel and the oscillograph was established by a pilot's signal which appeared on both recording devices and by marks on the oscillogram which indicated the frames being taken by the movie camera.

The automatic observer panel recorded the airspeed and altitude from the production pressure sensors: a "dog-leg" total pressure tube and static pressure ports which were located on the lower portion of the nose of the aircraft. No other instruments were plumbed into the airspeed system and the pressure lines were as short as possible in order to keep airspeed lag small. The automatic observer panel also included a "fuel remaining" gage and an engine speed indicator. All instruments were calibrated before the test program.

The oscillograph recorded time histories of the longitudinal and vertical

accelerations at the aircraft center-of-gravity, pitching velocity, and boom angle-of-attack. To measure the angle-of-attack, a 100-inch boom with a flow vane near the tip was installed on the nose of the aircraft.

Free air temperature was determined from the regular, twice-a-day meteorological balloon soundings from San Nicolas Island and Point Mugu.

Test Procedure

At each of the three test altitudes; 10 000, 25 000 and 35 000 feet, and at Mach number increments of 0.1, windup turns and pushover-pullups were conducted to and through the stall. The windup turns were done slowly to establish the maximum lift coefficient for a near zero angle-of-attack rate, while the pushover-pullups were done to obtain various pitch rates. Pushovers to zero g's were performed in order to assure a uniform starting condition and no separation prior to the test.

Measurement Errors

The errors (root-mean-square values) were determined for a typical test point for the non-dimensional variables of interest as tabulated below.

Mach number	1%
Reynolds number	2.5%
Lift coefficient	2.5%
Non-dimensional angle-of-attack rate	2%

DATA PROCESSING AND ANALYSIS

Figure 5 presents representative basic data for wing W-2. The data show typical curves of the lift coefficient versus the angle-of-attack for static and dynamic stalls and time histories of the angle-of-attack.

Examination of the wind tunnel data indicated large oscillations in the force data at low tunnel speeds. Figure 6 shows an extreme example of this phenomenon at two angle-of-attack rates. The largest peak-to-peak amplitude of the oscillation prior to the stall averaged over all the dynamic runs at each Mach and Reynolds number is given in Figure 7. As shown, the amplitude was low above Mach 0.4 but increased rapidly at low Mach numbers.

Consideration was given to discarding the few runs where the oscillations were large. Since a pair of runs was performed at each angle-of-attack rate, it was possible to compare the degree of repeatability. These data are also presented in Figure 7 in terms of the fractional spread in the maximum lift coefficients between data points. Note that the difference between a pair of points is only 0.03 on the average and that there is no increase at the low Mach numbers.

Another reason for not discarding the low Mach data was the belief that the large oscillations were due primarily to inertial reaction forces in the model and supporting structure which was undergoing small amplitude structural vibrations. The predominant frequency was slightly over 100 cps and this frequency remained about constant for all the high amplitude oscillations. Structures vibrating at these frequencies are nearly always dominated by inertia forces which increase as the square of the frequency.

The progressive increase in the maximum lift with the angle-of-attack rate is given in Figure 8 which is a replot of the faired curves of Figure 5. Note that angle-of-attack rate changes the slope and position of the lift curve only slightly at low values of the lift, but does extend the lift curve to considerably higher values.

The next step in processing the wind tunnel data was to plot the maximum lift coefficient from the lift versus angle-of-attack curves against the non-dimensional angle-of-attack rates. Figures 9 through 14 are plots of the wind tunnel data presented in this manner. In fairing the curves, the static stall point was favored, but in a few cases, crossplots of the figures suggested a revised fairing which did not favor the static stall point.

Figure 15 presents crossplots of Figures 9 through 14. The data in Figure 15 were replotted in Figures 16 through 19 to aid the discussion to follow.

The basic flight data were time histories of which Figure 20 is an example. The variation in airspeed and altitude is typical. The tests were conducted to achieve the desired values of airspeed and altitude at the moment maximum lift was achieved.

The non-dimensional parameters of interest were calculated from the basic flight data and replotted against the angle-of-attack as in the example of Figure 22. Since aerodynamic theory indicates that the wing lift acts at the one-quarter chord point and is determined by the downwash at the three-quarter chord point, the flight test data were plotted against the angle of attack at the three-quarter chord point. To obtain this value of the angle-of-attack, the indicated angle-of-attack was corrected for boom upwash by the relationship discussed in Reference 5:

$$\alpha_f = \frac{\alpha_i}{\left[1 + \left(\frac{R_{boom}}{R_{vane}}\right)^2\right]}$$

where R is the radius. A distributed load proportional to the boom weight was applied and the deflection angle at the flow vane measured to obtain a correction for boom bending:

$$\alpha_b = \alpha_f + 0.14 \left(a_z - 1 \right)$$

where a_z is the normal acceleration in g's and α_b is the true boom angle-of-attack in degrees. The position error was found to be negligible. Vane asymmetry could have resulted in a large error, but no correction was applied since this error is typically a constant at all values of the angle-of-attack (Reference 5) and hence does not affect the angle-of-attack rate. Finally, the value of the angle-of-attack at the three-quarter chord point was calculated from the relationship:

$$\alpha_{3/4\,\bar{c}} = \alpha_b + \frac{x}{V} \frac{d\theta}{dt}$$

where x is the distance from the wing three-quarter chord point to the flow vane location on the boom (242 inches).

The angle-of-attack rates were determined from the angle-of-attack time history prior to and at stall. Each of the flight data points was obtained from the time derivative of a quadratic function fitted to seven points equally distributed and neighboring the data point being reduced. The seven points spanned roughly a one-second time interval. Figure 21 is a typical flight stall and shows that, generally, the angle-of-attack rate was nearly constant preceding stall.

Various definitions of the angle-of-attack rate have been used in other investigations which try to account for the angle-of-attack history prior to stall by some sort of an average. In Reference 1 the rate was taken from the slope of a line joining the angle-of-attack curve at points corresponding to zero and maximum lift. Another method of accounting for the angle-of-attack history is to fit a polynominal to the data points and take the second, third, etc. derivatives at some point preceding stall. In this report, however, the first derivative just prior to stall appeared to be sufficient for the flight data. The wind tunnel data presented no difficulties in defining an angle-of-attack rate for stall since the angle-of-attack rate was constant well before the stall (Figures 6 and 7 show typical examples).

In calculating the lift coefficient from the flight data, use was made of the longitudinal acceleration data. Also the component of the engine thrust directed up along the lift vector was subtracted before the lift coefficient was calculated. The thrust was taken from a non-dimensional engine curve at the engine speed read from the flight records. The engine curves were derived during early flight programs with the T-1A airplane.

A brief analysis was made of the incremental lift due to the tail and the fuselage. Both were found to be negligible partly because of a favorable location of the center of gravity near the 25% chord point.

The data describing the stall points were taken from curves such as those given in Figure 21 and are presented in Figure 22. The Mach and Reynolds

numbers listed in the figure are averages with variances less than 0.01 and 0.5 x 10^6, respectively.

The flight data in Figure 22 were crossplotted in Figure 23 at constant values of the angle-of-attack rate. The plot also includes wind tunnel data for the W-2 wing. This model was similar to the wing of the test airplane except the taper ratio was 1.00 instead of 0.38 and the geometric twist was 0 instead of -1.5 degrees. The data in Figure 23 was grouped according to Reynolds number. Curves of constant Reynolds numbers are presented at values of 1.4, 2.8, 8.6 and 12.0 x 10^6. The variance in Reynolds number is 18, 10, 8 and 14%, respectively. Two points, at Reynolds numbers of 18.5 and 21.1 x 10^6, were not grouped with any other points.

RESULTS AND DISCUSSION

General

Wind tunnel and flight test data showing the effect of angle-of-attack rate on the maximum lift coefficient, $C_{L_{max}}$, are presented in Figures 9 through 14 and Figure 22. In spite of considerable scatter, $C_{L_{max}}$ shows a generally linear increase with increasing non-dimensional angle-of-attack rate, $\frac{\bar{c}}{V}\dot{\alpha}$.

The generally linear trend has been found before; as, for example, in Reference 1 which appears to be the most thorough investigation of the effect of $\frac{\bar{c}}{V}\dot{\alpha}$ on $C_{L_{max}}$ previously undertaken. However, in this reference a limiting value of $C_{L_{max}}$ was reached (which decreased with increasing Mach number) after which $C_{L_{max}}$ remained constant with further increases in $\frac{\bar{c}}{V}\dot{\alpha}$. It is suspected that the appearance or non-appearance of a limit $C_{L_{max}}$ might depend on the airfoil section being tested. No limit $C_{L_{max}}$ appears in the data reported herein for flight and tunnel tests of wings with 65_1-XXX (a = .5) airfoil sections up to $\frac{\bar{c}}{V}\dot{\alpha}$ = 0.047. Reference 1 investigated a wing model with a modified NASA 230- series section and showed limiting values of $C_{L_{max}}$. Reference 2 reported on flight tests of an airplane with a 66,2- (1.8) (15.5) (a = .6) root wing section and a 66,1- (1.8) (12) (a = .6) tip section and did not show any limiting values of $C_{L_{max}}$ up to $\frac{\bar{c}}{V}\dot{\alpha}$ = 0.0115. Hence 65_1- series section appear to behave similarly to 66,1- and 66,2- series section. In Reference 3, however, limiting values were reported from flight tests of a wing with a 66,2X-116 (a = .6) root section and a 66,2X-216 (a = .6) tip section. It would appear that this reference would disprove the dependency on section characteristics; however, it may be the 66,2X series sections differed sufficiently from 65_1-, 66,1- and 66,2- series sections to result in the appearance of limiting values of $C_{L_{max}}$ such as also were observed for the 230- series section.

Another factor investigated was the slope $d\left(C_{L_{max}}\right) / d\left(\frac{\bar{c}}{V}\dot{\alpha}\right)$.

The slopes found in both the wind tunnel and the flight test data were in general less than those reported in References 2 and 3 for flight tests and far less than the slopes found in wind tunnel tests of a modified 230 series section, Reference 2, being only one-fourth to one-third as large. It appears the slopes are related to the existence of a limit $C_{L_{max}}$ in the sense that a limit $C_{L_{max}}$ appears whenever the slope $d\left(C_{L_{max}}\right) / d\left(\frac{\bar{c}\dot{\alpha}}{V}\right)$ is high. A limit $C_{L_{max}}$ might be reached even for those cases where the values of the slopes were small if tests at exceptionally high $\frac{\bar{c}}{V}\dot{\alpha}$ were conducted.

A significant exception to the generally increasing $C_{L_{max}}$ with increase in $\frac{\bar{c}}{V}\dot{\alpha}$ was found in the wind tunnel data. This was a "hump" in the $C_{L_{max}}$ versus $\frac{\bar{c}}{V}\dot{\alpha}$ curves at low values of the angle-of-attack rate which occurred for certain configurations at Mach numbers near 0.6 (Figures 9, 10, 12 and 14). It is felt the "hump" cannot be dismissed as data scatter since it was repetitious and occurred for three different wing configurations. Another exception to linearity was found in the flight test data at Mach 0.57 and Reynolds number 21.1 x 10^6 (Figure 22), the highest Reynolds number tested. In this case, a decrease in $C_{L_{max}}$ was observed. The maximum $\frac{\bar{c}}{V}\dot{\alpha}$ was low and it may be a "hump" effect would have appeared if the airplane could have been tested at higher angle-of-attack rates.

Parameter Variations

Tests were conducted to determine the sensitivity of the effect of $\dot{\alpha}$ on $C_{L_{max}}$ to various parameter changes. To this end the aerodynamic variables (Mach and Reynolds number), as well as the wing configuration variables (thickness, camber, aspect ratio, and sweep angle) were varied.

Mach Number. - In Figure 16, $C_{L_{max}}$ is plotted versus Mach number for values of $\frac{\bar{c}}{V}\dot{\alpha}$ equal to 0 and 0.01. It can be seen that in general the trends are similar both for a $\frac{\bar{c}}{V}\dot{\alpha}$ of 0 and 0.01; namely, an initial decrease in $C_{L_{max}}$ with increasing Mach number followed by a secondary peak. The same trend also exists in the flight data as Figure 23 demonstrates. This is in agreement with the trends found in Reference 3 where it was felt that the secondary peak was caused by a broadening of the upper surface low pressure region which offset the reduction in the negative pressure peak as Mach number increased. The reference implies that the reduction in peak pressures delayed stall separation until higher values of $C_{L_{max}}$ were reached.

Although $C_{L_{max}}$ for both steady-state and $\frac{\bar{c}}{V}\dot{\alpha} = 0.01$ vary considerably with Mach number, the difference between them (i.e., the increase in

$C_{L_{max}}$ due to a $\frac{\bar{c}}{V}\dot{\alpha}$ of 0.01) remains fairly constant with Mach number. This result differs from that found in Reference 1 where $\frac{\bar{c}}{V}\dot{\alpha}$ had no effect on $C_{L_{max}}$ for Mach numbers greater than 0.6.

Reynolds Number. - The wind tunnel models were each tested at two Reynolds numbers, 1.4×10^6 and 2.8×10^6 (2.8 and 5.6×10^6 for the model having a low aspect ratio). In Figure 15 it can be seen that an increase in Reynolds number generally caused an increase in $C_{L_{max}}$ for both $\frac{\bar{c}}{V}\dot{\alpha} = 0$ and 0.01. In most cases this increase in $C_{L_{max}}$ is roughly the same for $\frac{\bar{c}}{V}\dot{\alpha} = 0.01$ as for $\frac{\bar{c}}{V}\dot{\alpha} = 0$; the incremental increase in $C_{L_{max}}$ due to $\frac{\bar{c}}{V}\dot{\alpha}$ thus remaining relatively unaffected by Reynolds number. The flight test data, although somewhat sparse, indicate a similar trend for the higher Reynolds numbers (Figure 23).

Thickness Ratio. - Figure 16 shows that increasing the thickness ratio from 13 to 16% had a smaller effect on the increase in $C_{L_{max}}$ with $\frac{\bar{c}}{V}\dot{\alpha}$ compared to decreasing the thickness ratio from 13 to 9%. There is reason to believe the type of stall changed going from 13 to 9% since Figure 15 shows a decrease in maximum lift as Reynolds number is increased. This unusual behavior with Reynolds number was also observed to a lesser degree for wing W-5, which has a sweepback of 35 degrees as Figure 15 shows. With sweepback, the streamwise sections become thinner and an effect roughly equivalent to a thinner wing without sweepback would be expected.

Airfoil Camber. - Airfoil camber had the largest effect on the ability $\frac{\bar{c}}{V}\dot{\alpha}$ to increase $C_{L_{max}}$. Figure 17 shows how the effect of $\frac{\bar{c}}{V}\dot{\alpha}$ on $C_{L_{max}}$ is greatly reduced by increasing the camber of the wing.

Apparent camber was investigated to determine if this factor could be largely responsible for the increase in maximum lift with angle-of-attack rate.

In potential flow it is known that pitching velocity can be considered equivalent to a parabolic camber with vertex at the axis of rotation (Reference 6). From experiment it is known that increasing the camber of an airfoil increases its maximum lift, for example see Reference 7. Figure 17 gives an indication of the amount of incremental change in $C_{L_{max}}$ of an uncambered wing due to $\frac{\bar{c}}{V}\dot{\alpha}$ that could be attributable to its having an "apparent camber". The apparent camber of wing W-6 undergoing a pitching velocity of $\frac{\bar{c}}{V}\dot{\alpha} = 0.01$ was computed from potential flow theory as follows:

$$\text{apparent camber} = \frac{1}{8}\frac{\bar{c}}{V}\dot{\alpha} = \frac{0.01}{8} = 0.00125$$

The difference in $C_{L_{max}}$ due to geometric camber can be obtained from the data for wings W-2 and W-6 which had cambers of 0.011 and 0, respectively. The effect of apparent camber on $C_{L_{max}}$ was assumed to be similar to that due to geometric camber and also that a linear increase occurs. Hence the increment in $C_{L_{max}}$ due to apparent camber is 0.00125/0.011 of the static lift increment between wings W-2 and W-6. It is seen in Figure 17 that the apparent camber effect accounts for only a small part of the increase in $C_{L_{max}}$ due to a $\frac{\bar{c}}{V}\dot{\alpha}$ of 0.01. While the camber of wing W-2 is not parabolic it was felt that the analysis sufficed for an order of magnitude answer.

Sweep Angle. - As seen from Figure 18, increasing the wing sweep angle greatly increases the effect of $\frac{\bar{c}}{V}\dot{\alpha}$ on $C_{L_{max}}$.

Aspect Ratio. - Figure 19 shows a limited comparison between the aspect ratio 3 and 6 models. No significant effect due to aspect ratio is evident.

CONCLUSIONS

The results of subsonic flight and wind tunnel tests on wings composed of NASA 65_1- series sections (65_1-213 section standard for comparison) led to the following conclusions for the range of Mach and Reynolds numbers, thickness ratio, camber, sweep and aspect ratio tested:

1. The increase in $C_{L_{max}}$ with $\frac{\bar{c}}{V}\dot{\alpha}$ was usually moderate (15-30%) and linear. No evidence of a limit in maximum lift appeared for values of $\frac{\bar{c}}{V}\dot{\alpha}$ up to 0.047. Near Mach 0.6 a "hump" effect sometimes appeared such that the maximum lift first increased rapidly with angle-of-attack rate, then decreased rapidly and then returned to the typically slow increase at higher rates.

2. Although Mach number had a considerable effect on static $C_{L_{max}}$, it generally had little effect on the incremental increase in maximum lift with angle-of-attack rate.

3. Increased Reynolds number usually increased $C_{L_{max}}$ and the amount of increase generally seemed to be unaffected by either Mach number or $\frac{\bar{c}}{V}\dot{\alpha}$.

4. Increasing wing thickness from 9% to 13% greatly reduced the effect of an angle-of-attack rate on maximum lift. An increase from 13% to 16% had a relatively small effect.

5. Increasing the camber from that corresponding to an ideal lift coefficient of 0 to one of 0.2 greatly reduced the effect of $\frac{\bar{c}}{V}\dot{\alpha}$ on incremental maximum lift.

6. Increasing the wing sweep from 0 to 35 degrees greatly increased the effect of angle-of-attack rate on maximum lift.

7. A limited comparison between wings of aspect ratios of 3 and 6 showed no significant effects attributable to aspect ratio.

8. The trends observed in the wind tunnel data were also observed in the flight data. For the most part, the magnitude of the maximum lift from the flight tests appears to agree with that from the wind tunnel tests. However, no direct comparison is possible due mainly to a difference in the Reynolds numbers tested.

Lockheed-California Company
Burbank, California
July 26, 1965

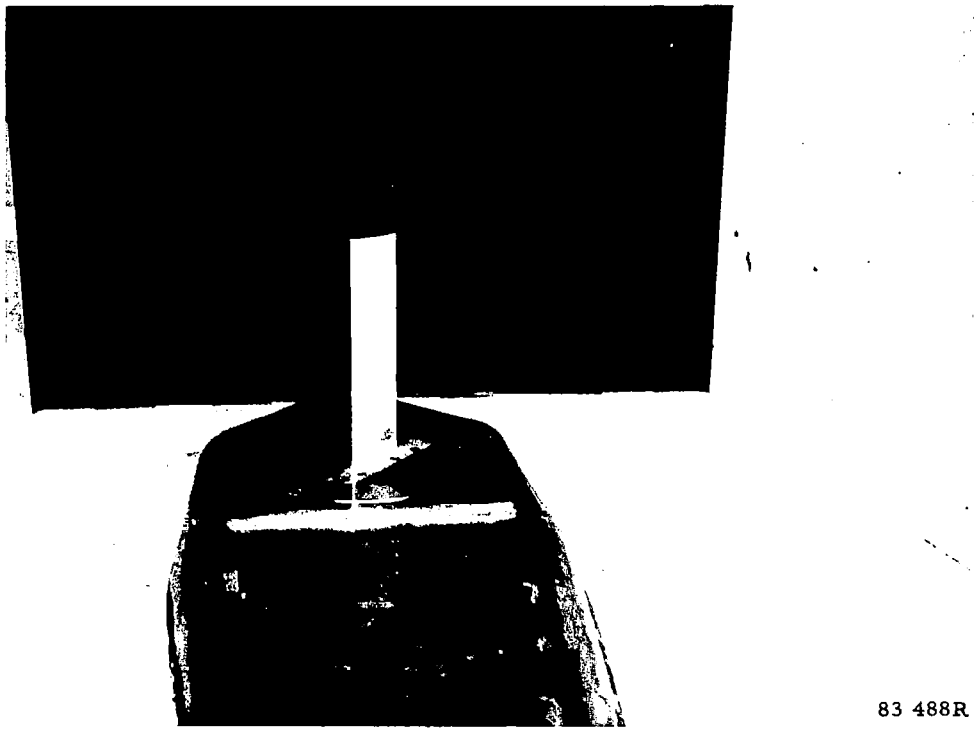

Figure 1. Wing W-2 Installed in Wind Tunnel

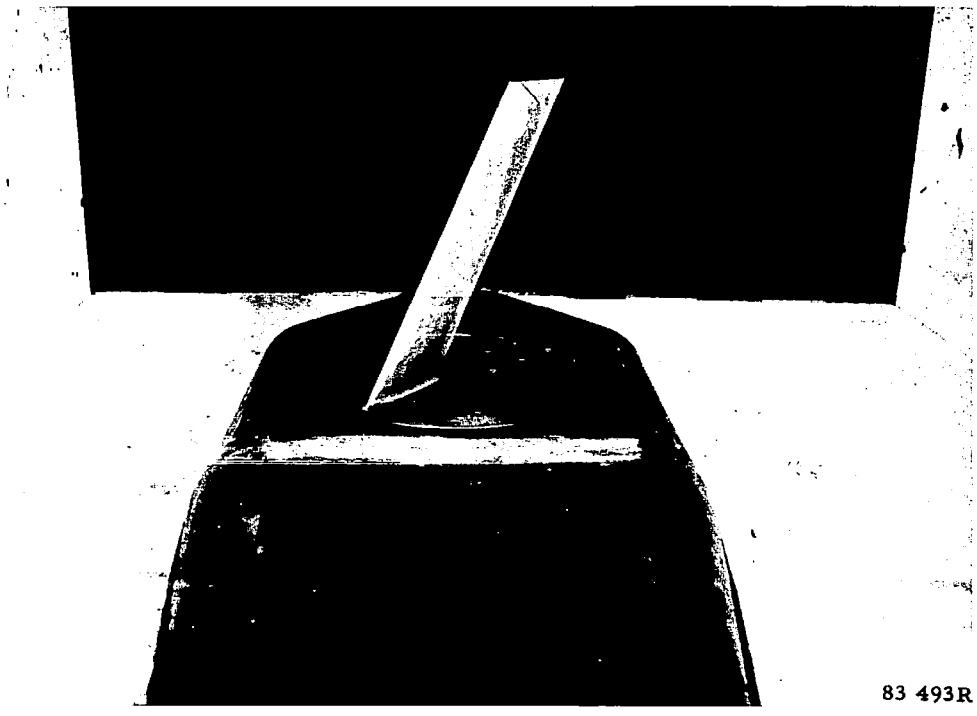

Figure 2. Wing W-5 Installed in Wind Tunnel

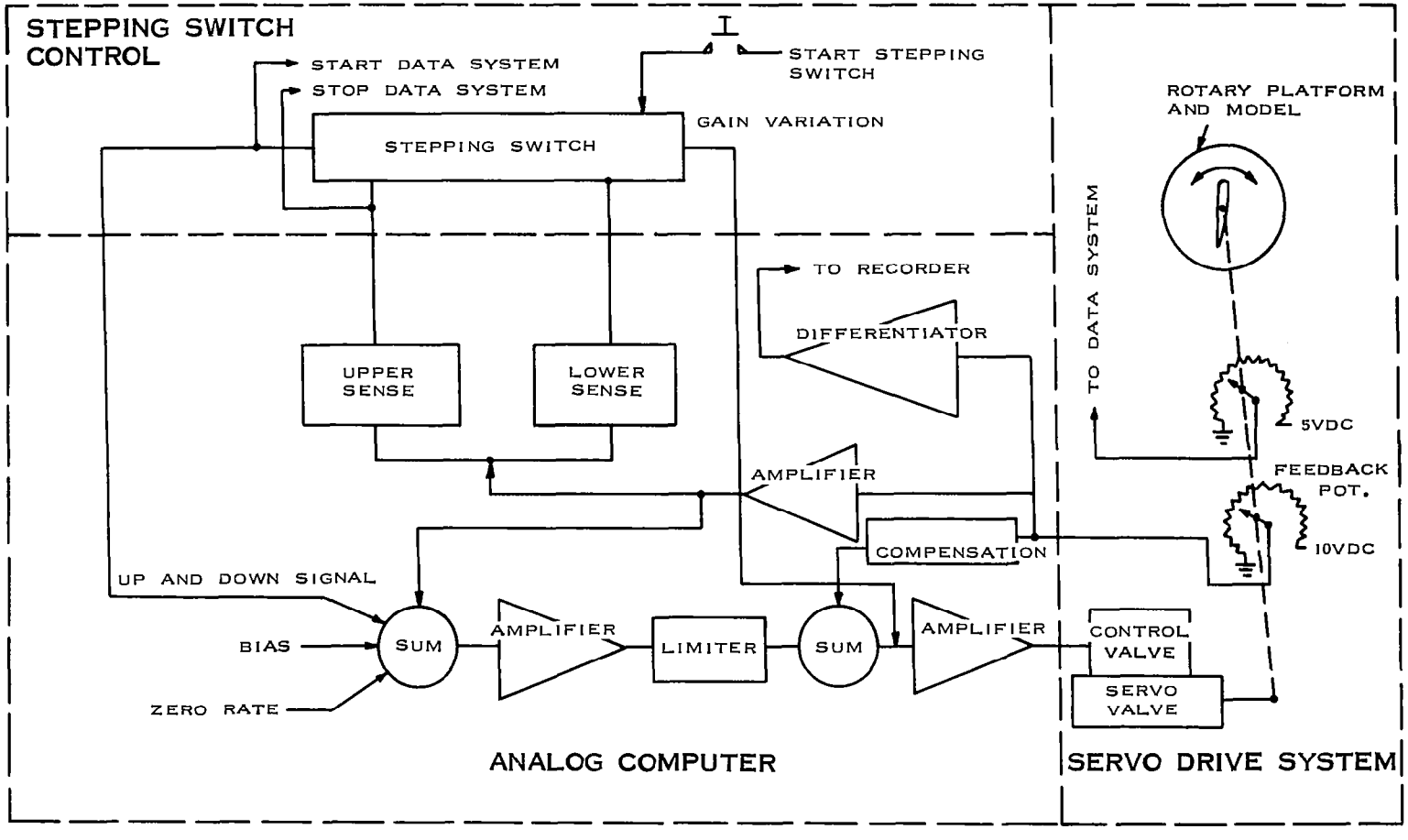

Figure 3. Block Diagram of Servo System

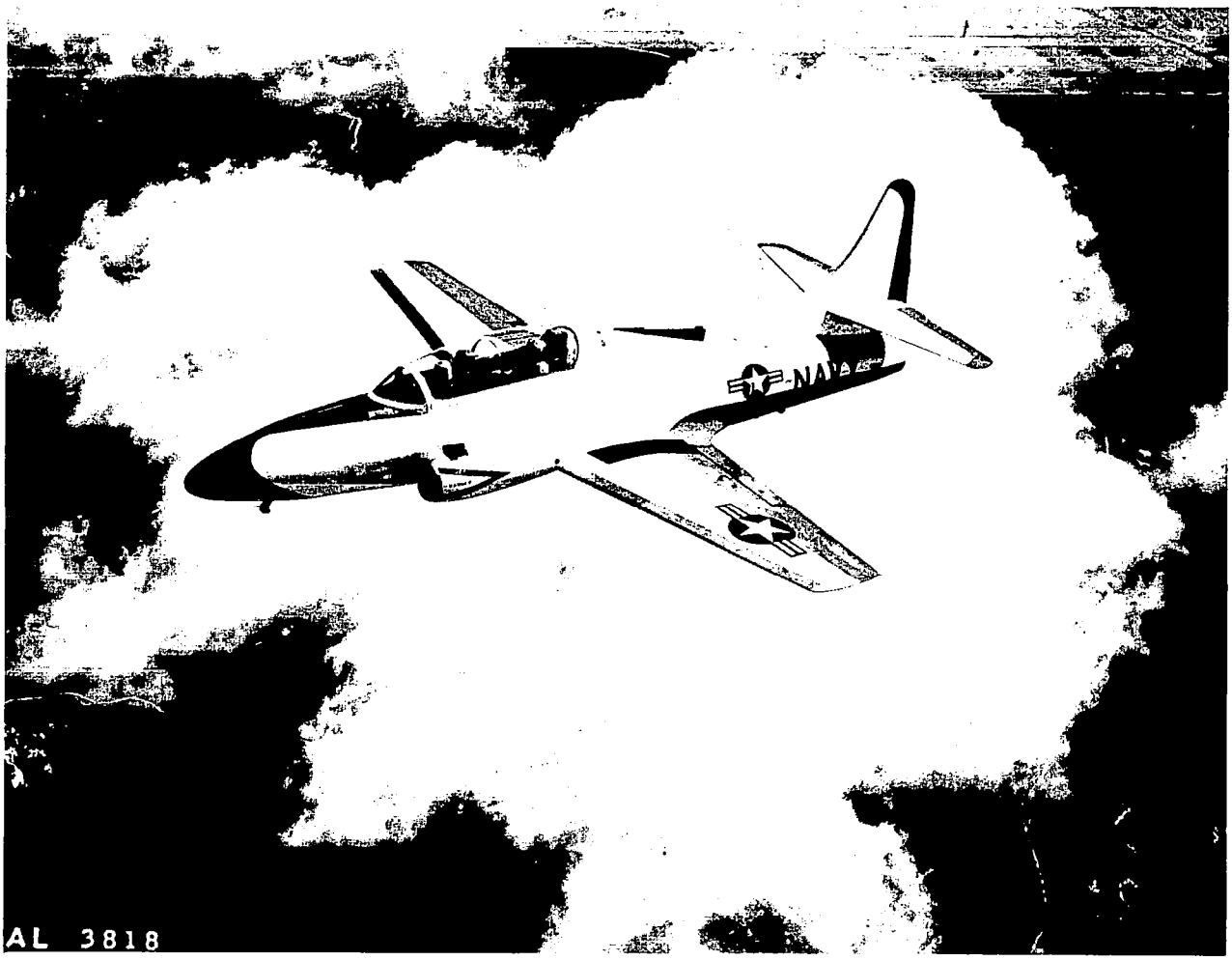

Figure 4. T-1A Airplane

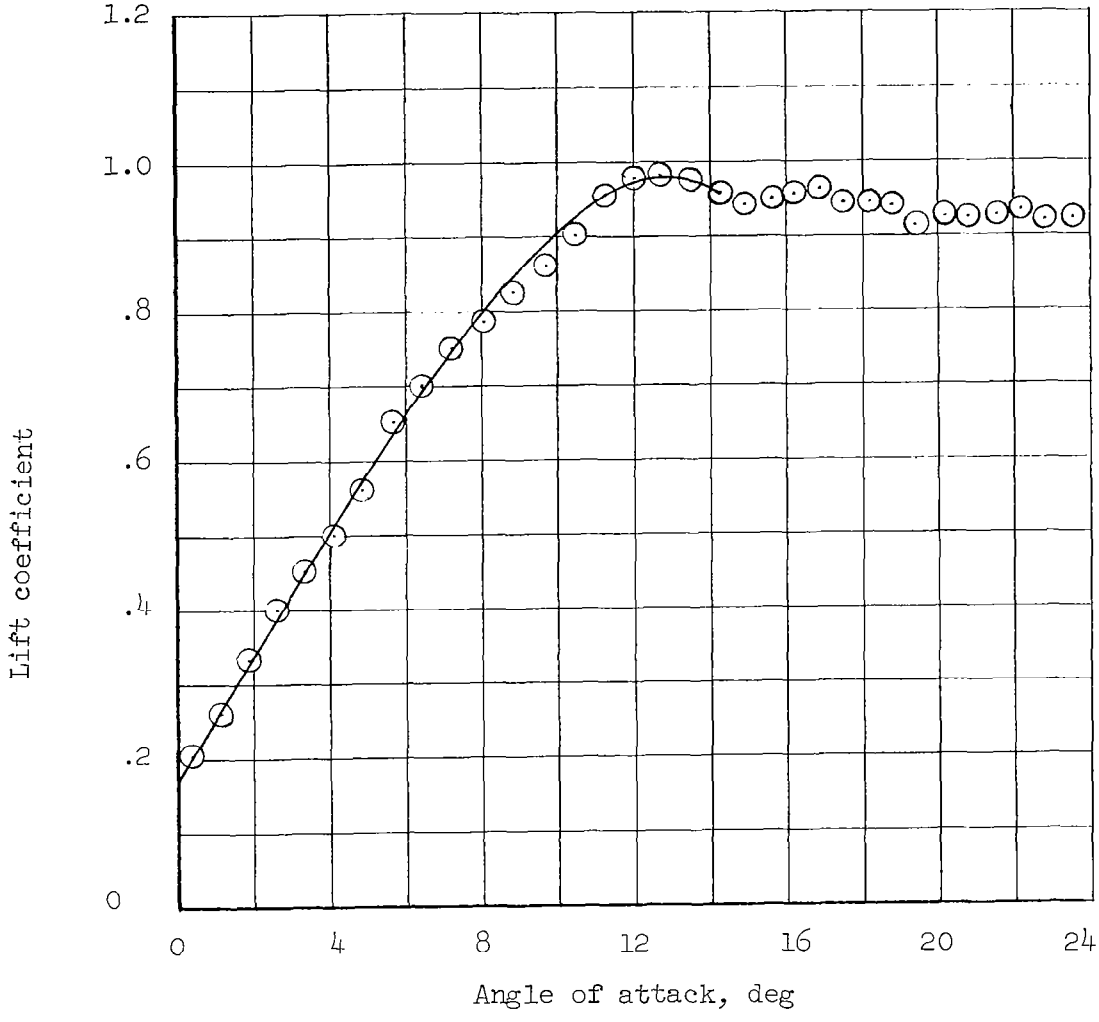

(a) $\frac{\bar{c}}{V}\frac{d\alpha}{dt} = 0$

Figure 5 -- Example of Wind Tunnel Data, M = .547, RN = 2.79 x 10^6, Wing W-2

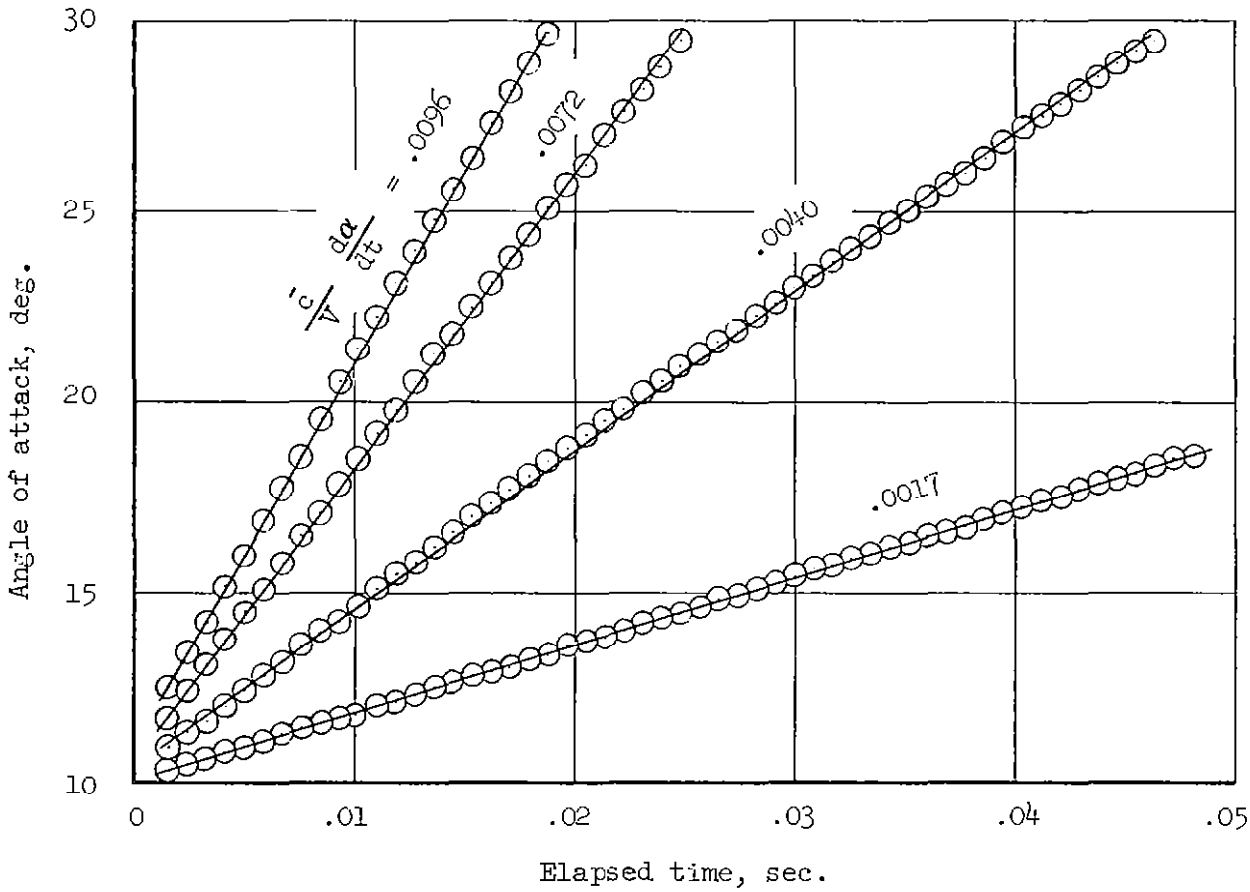

(b) Time history of angle of attack

Figure 5 -- Continued

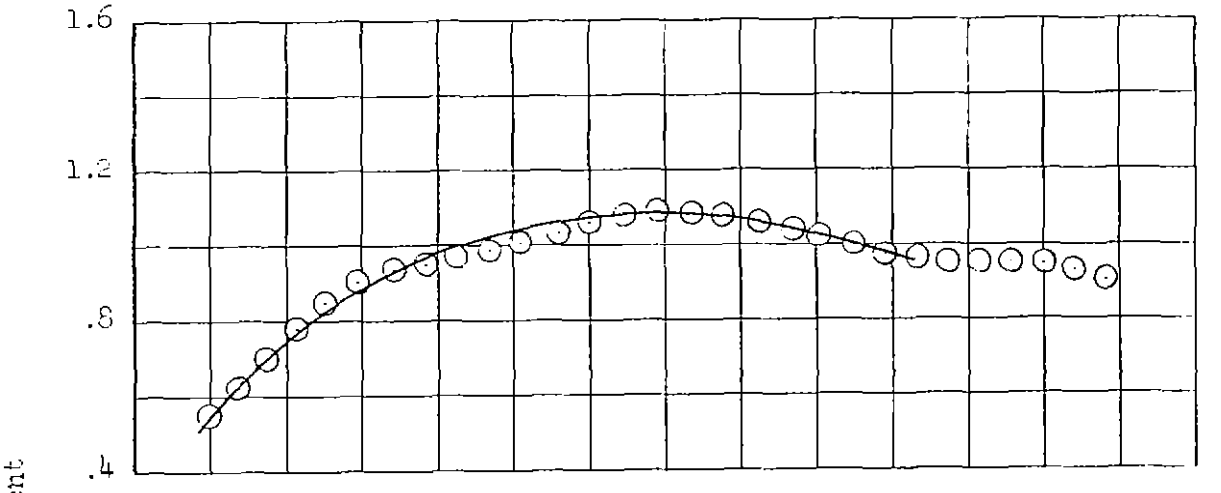

(c) $\frac{\bar{c}}{V}\frac{d\alpha}{dt} = .0096$

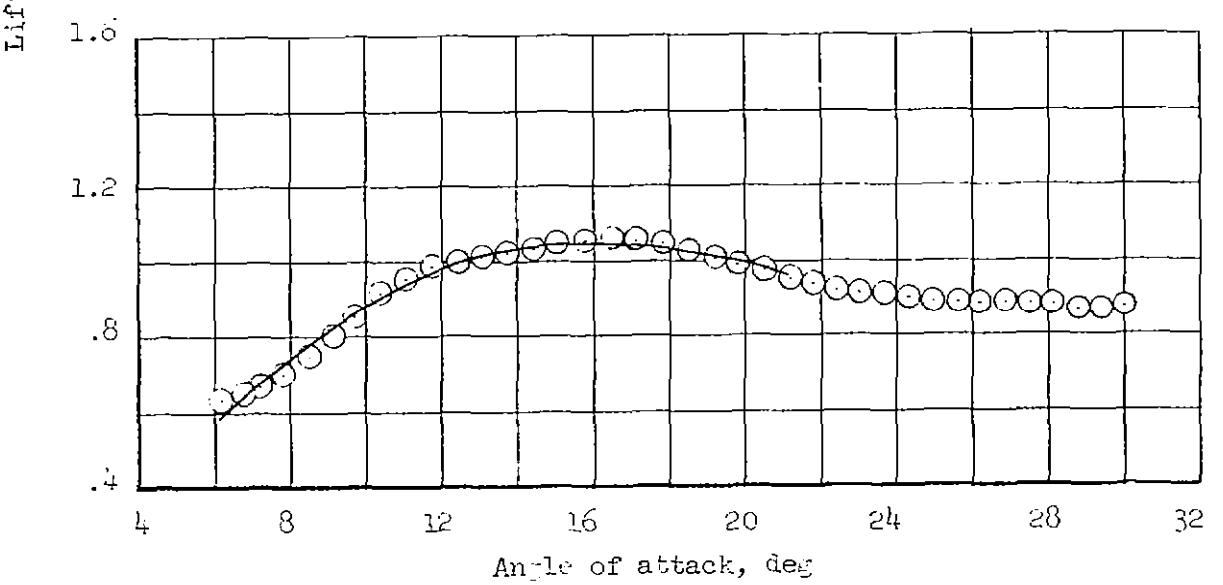

(d) $\frac{\bar{c}}{V}\frac{d\alpha}{dt} = .0072$

Figure 5 -- Continued

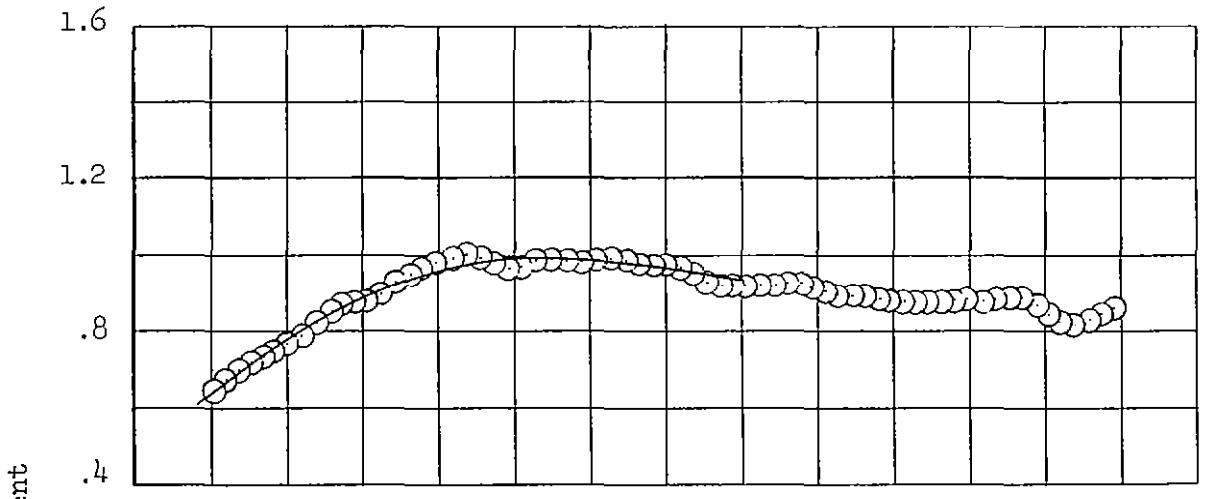

(e) $\frac{\bar{c}}{V}\frac{d\alpha}{dt} = .0040$

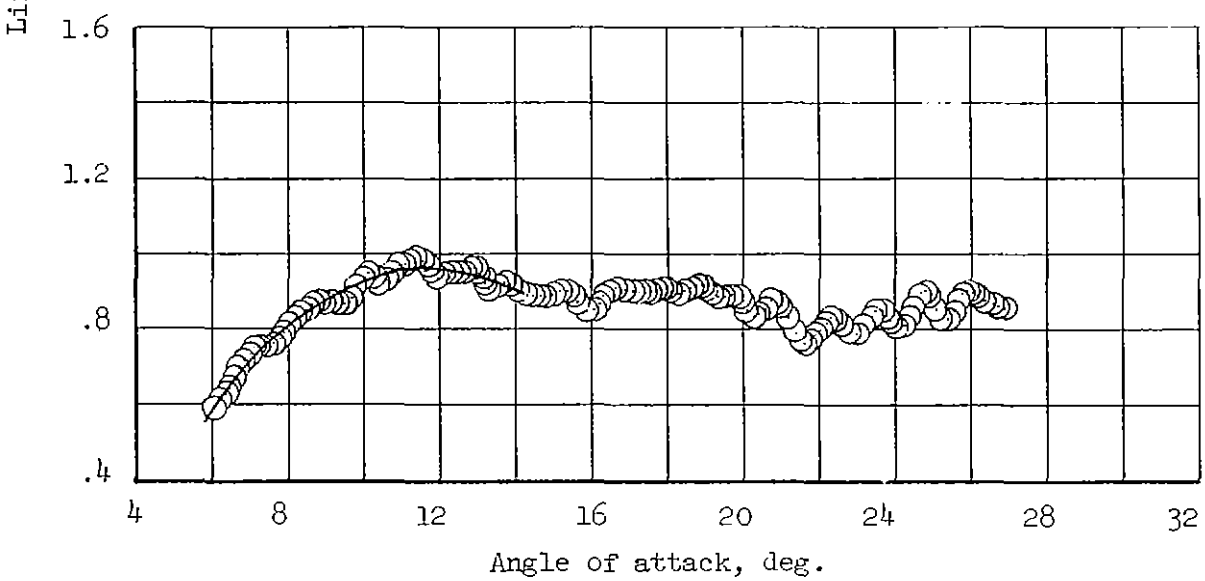

(f) $\frac{\bar{c}}{V}\frac{d\alpha}{dt} = .0017$

Figure 5 -- Concluded

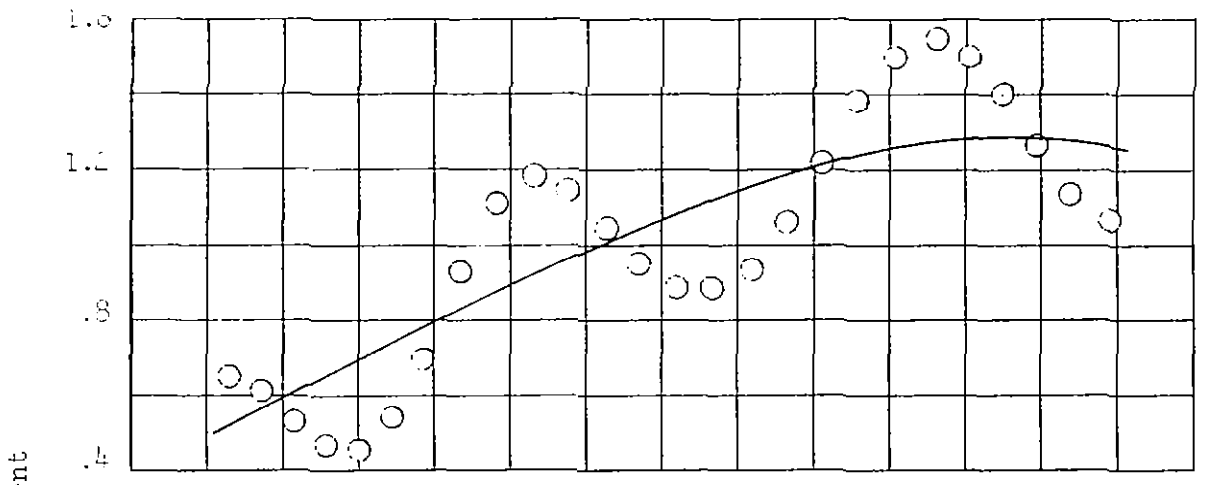

(a) $\frac{\bar{c}}{V}\frac{d\alpha}{dt} = .0238$

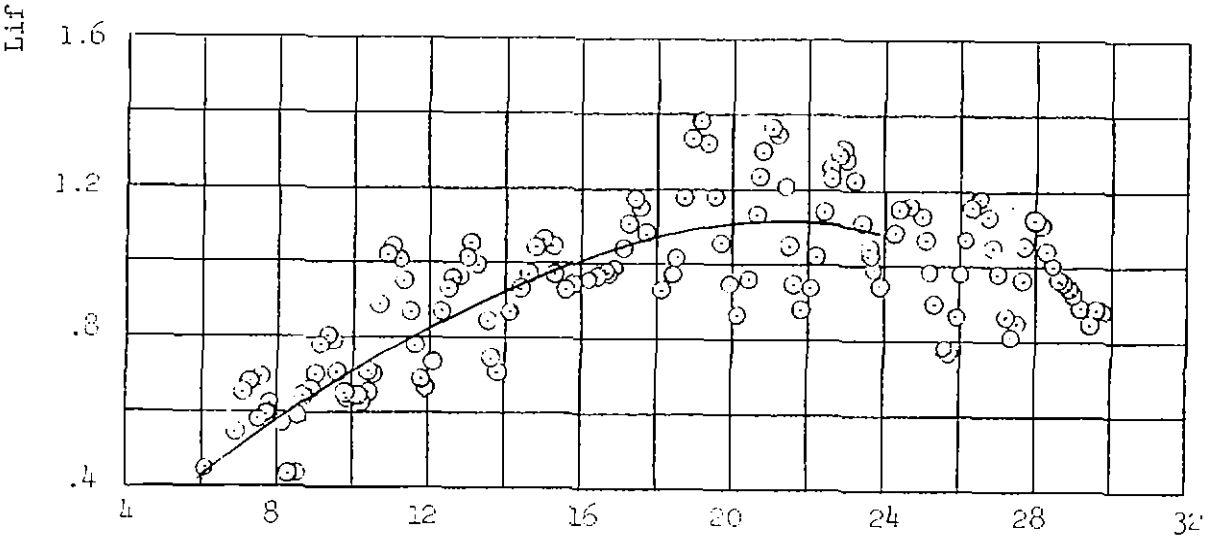

(b) $\frac{c}{V}\frac{d\alpha}{dt} = .0038$

Figure 6 -- Example of Wind Tunnel Data, M = .264. RN = 1.75×10^6, Wing W-2

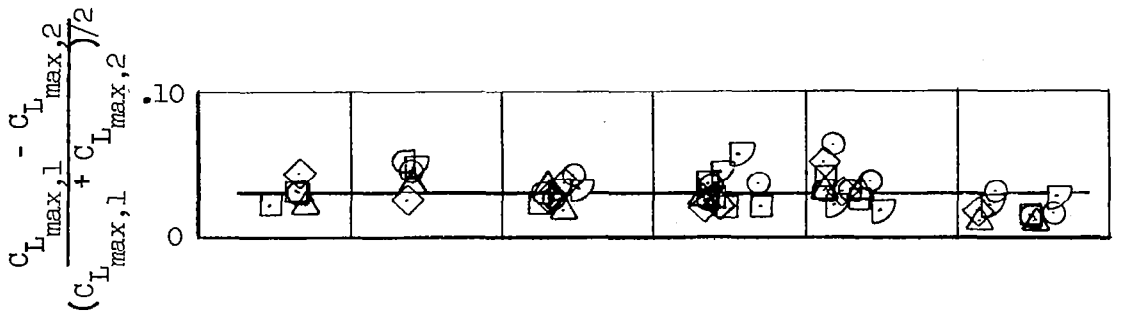

(a) Repeatability

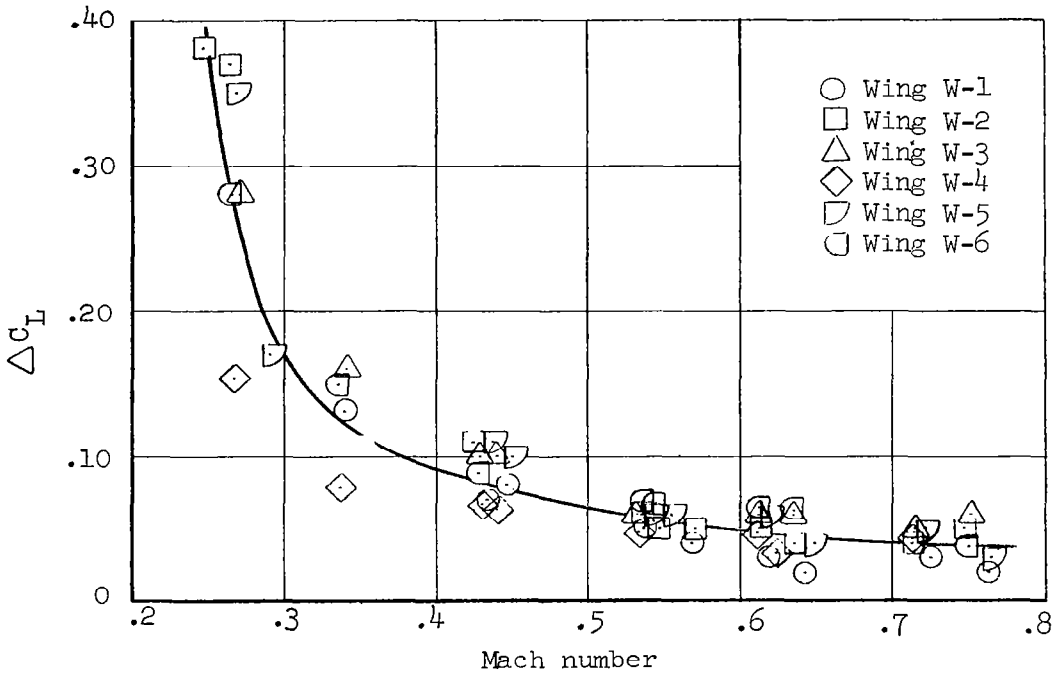

(b) Double Amplitude of Oscillations

Figure 7 -- Effect of Oscillations

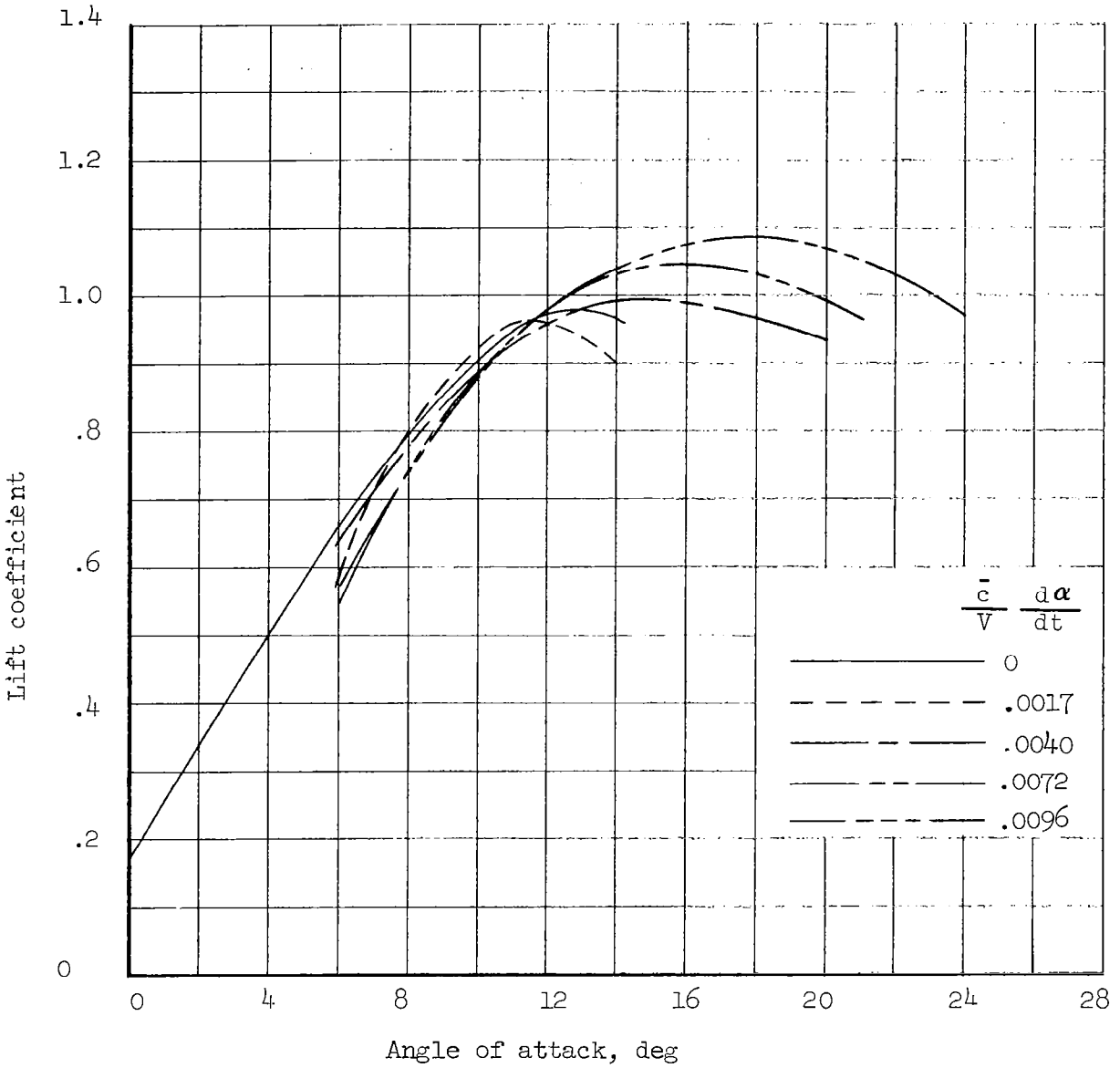

WING W-2, M = .547, RN = 2.79×10^6

Figure 8 -- Example of the Effect of Angle-of-Attack Rate on the Lift Curve

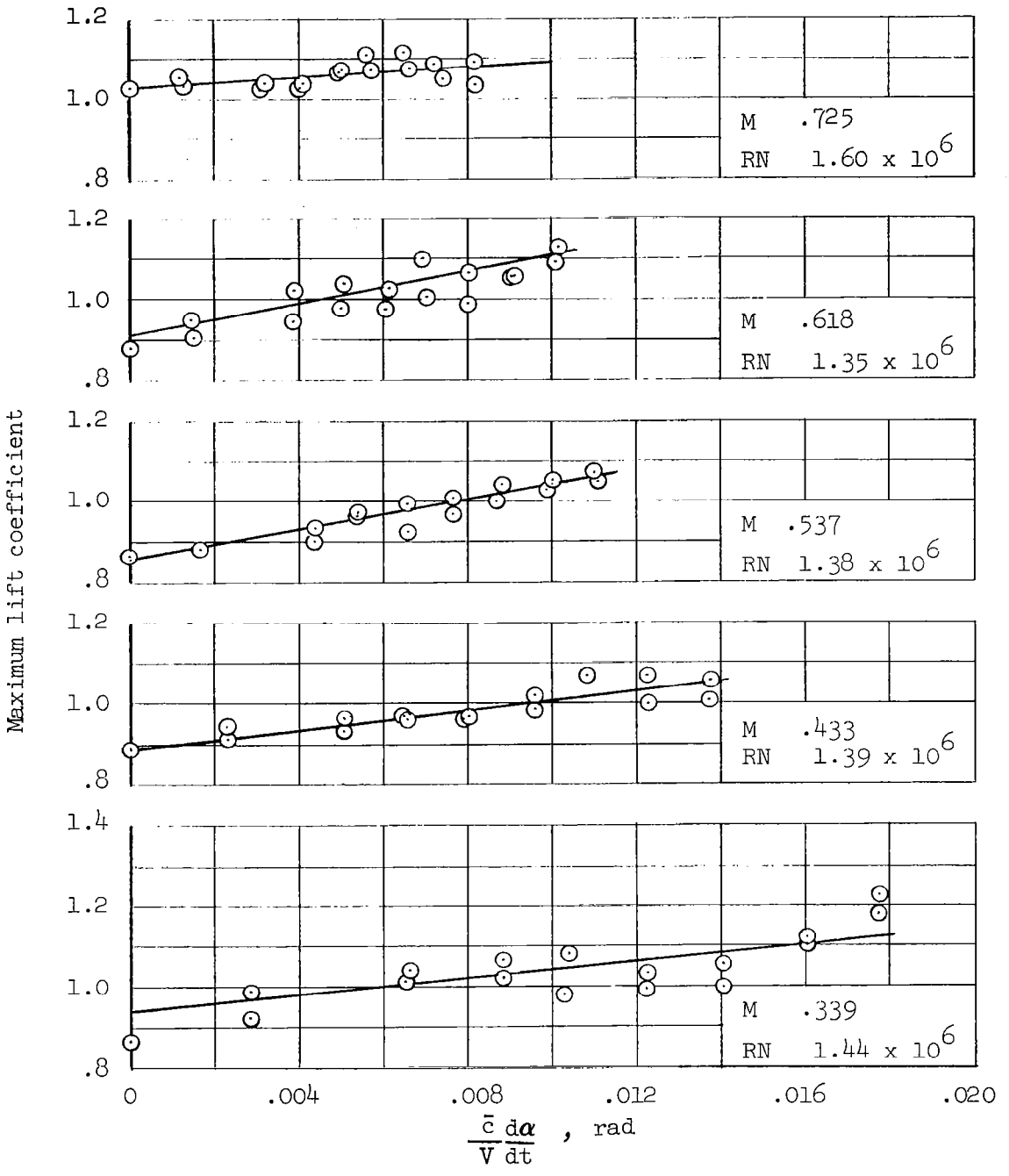

Figure 9 -- Effect of Angle-of-attack Rate on the Maximum Lift Coefficient of Wind Tunnel Wing W-1

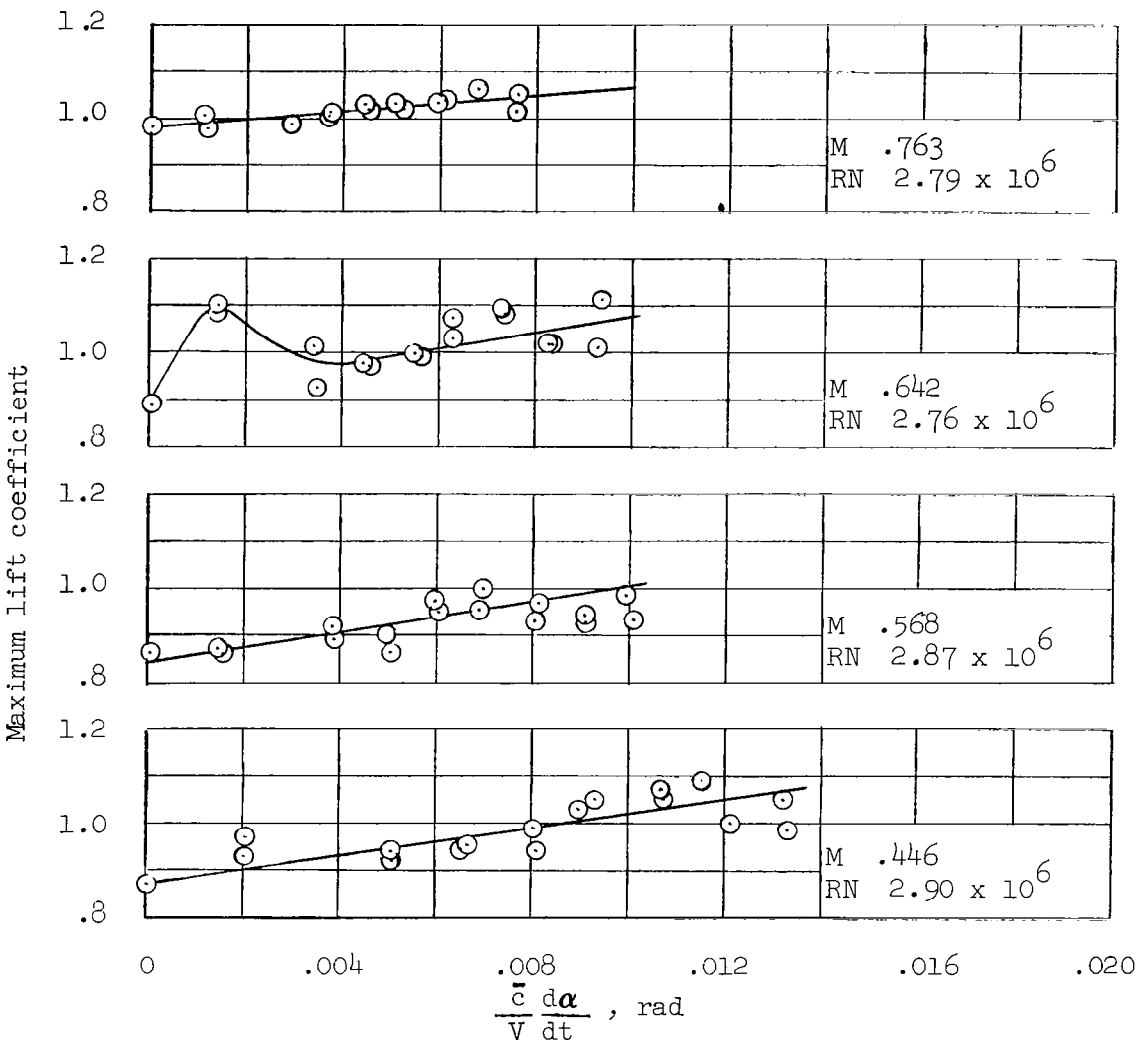

Figure 9 -- Concluded

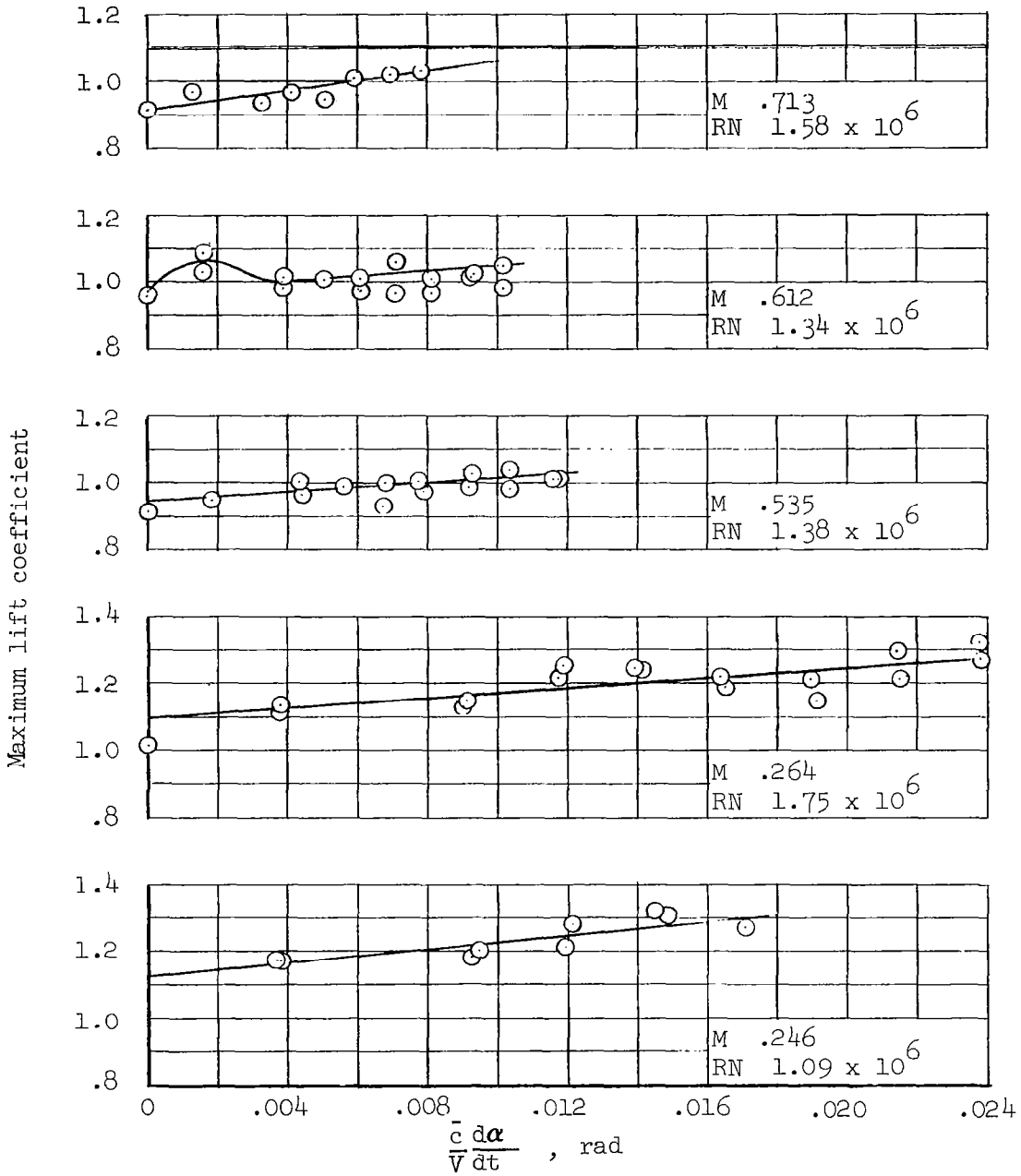

Figure 10 -- Effect of Angle-of-attack Rate on the Maximum Lift Coefficient of Wind Tunnel Wing W-2

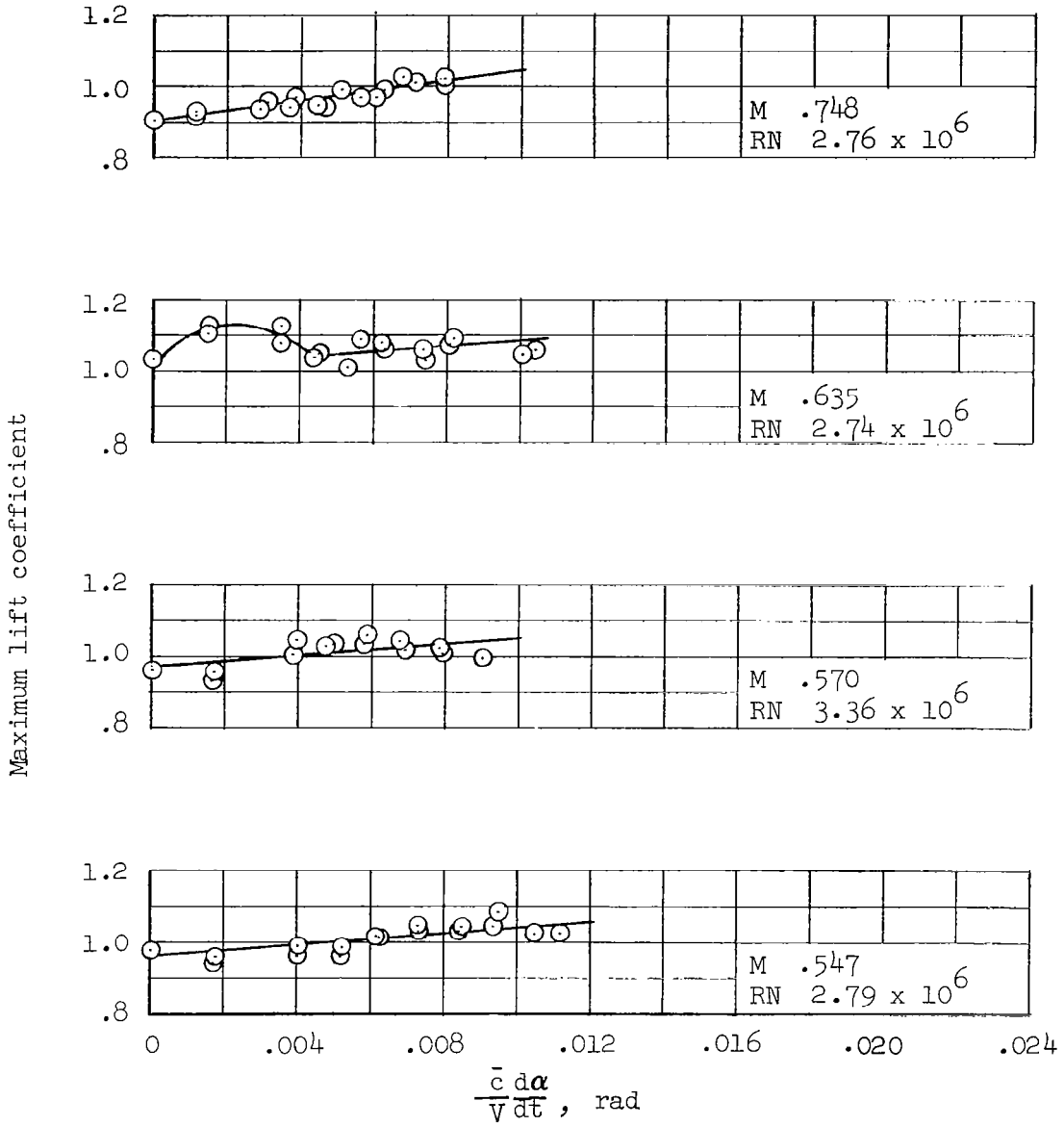

Figure 10 -- Concluded.

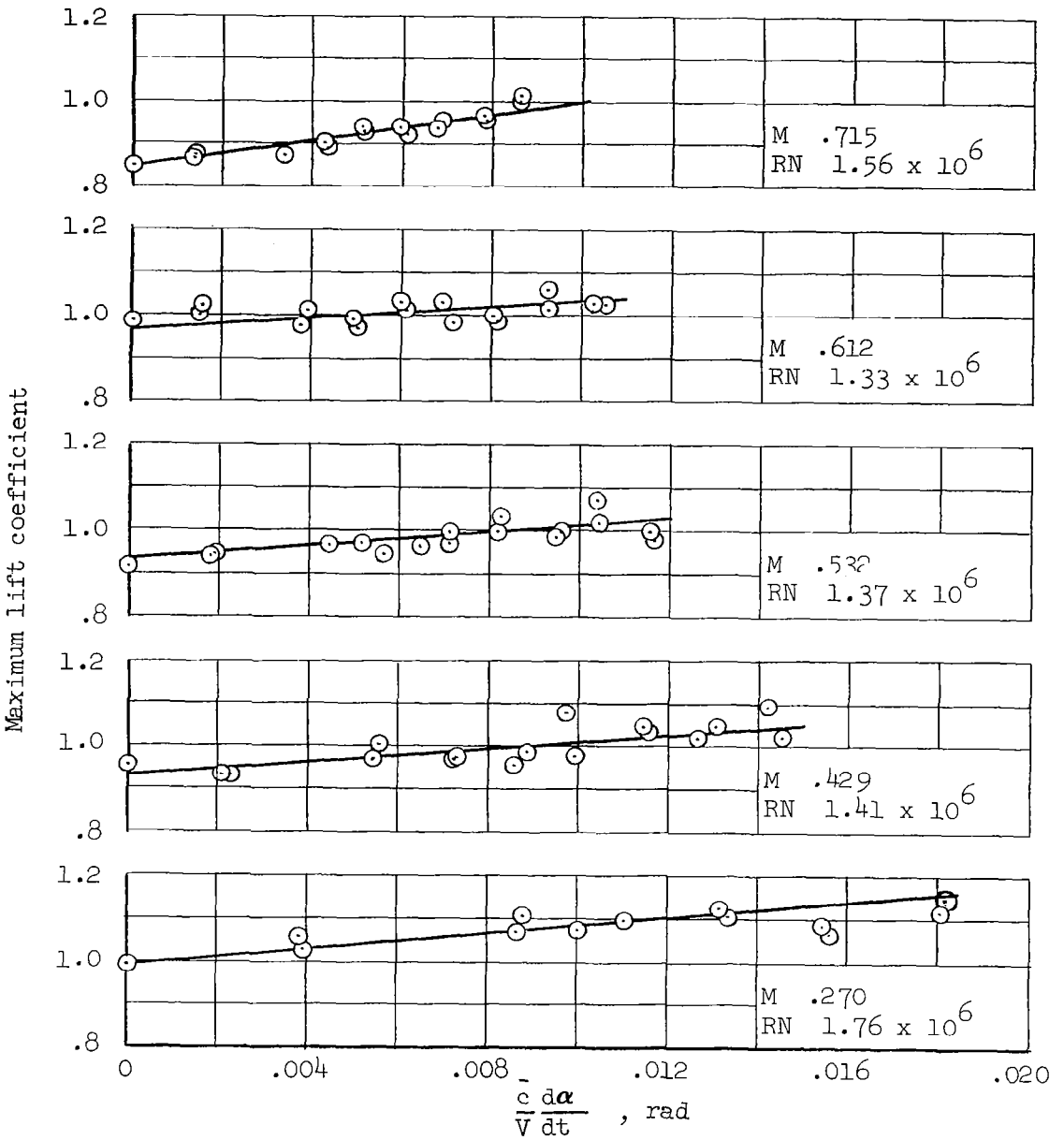

Figure 11 -- Effect of Angle-of-attack Rate on the Maximum Lift Coefficient of Wind Tunnel Wing W-3

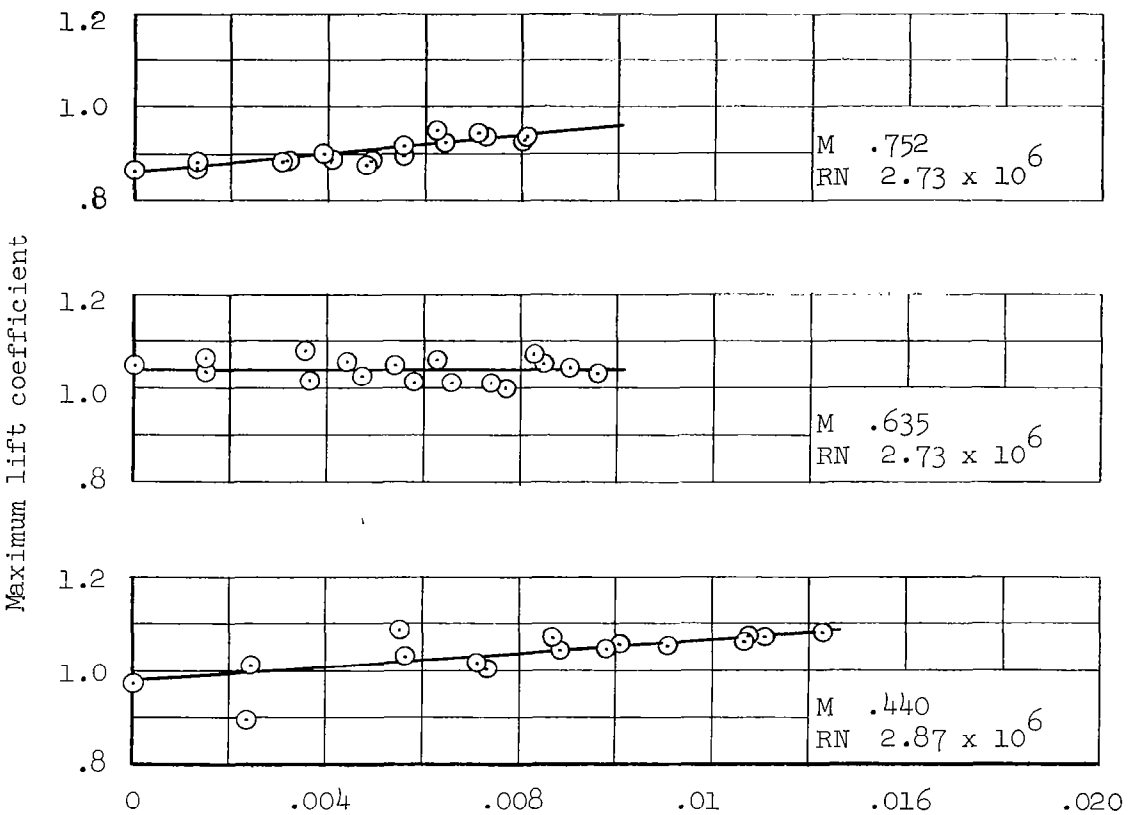

Figure 11 -- Concluded.

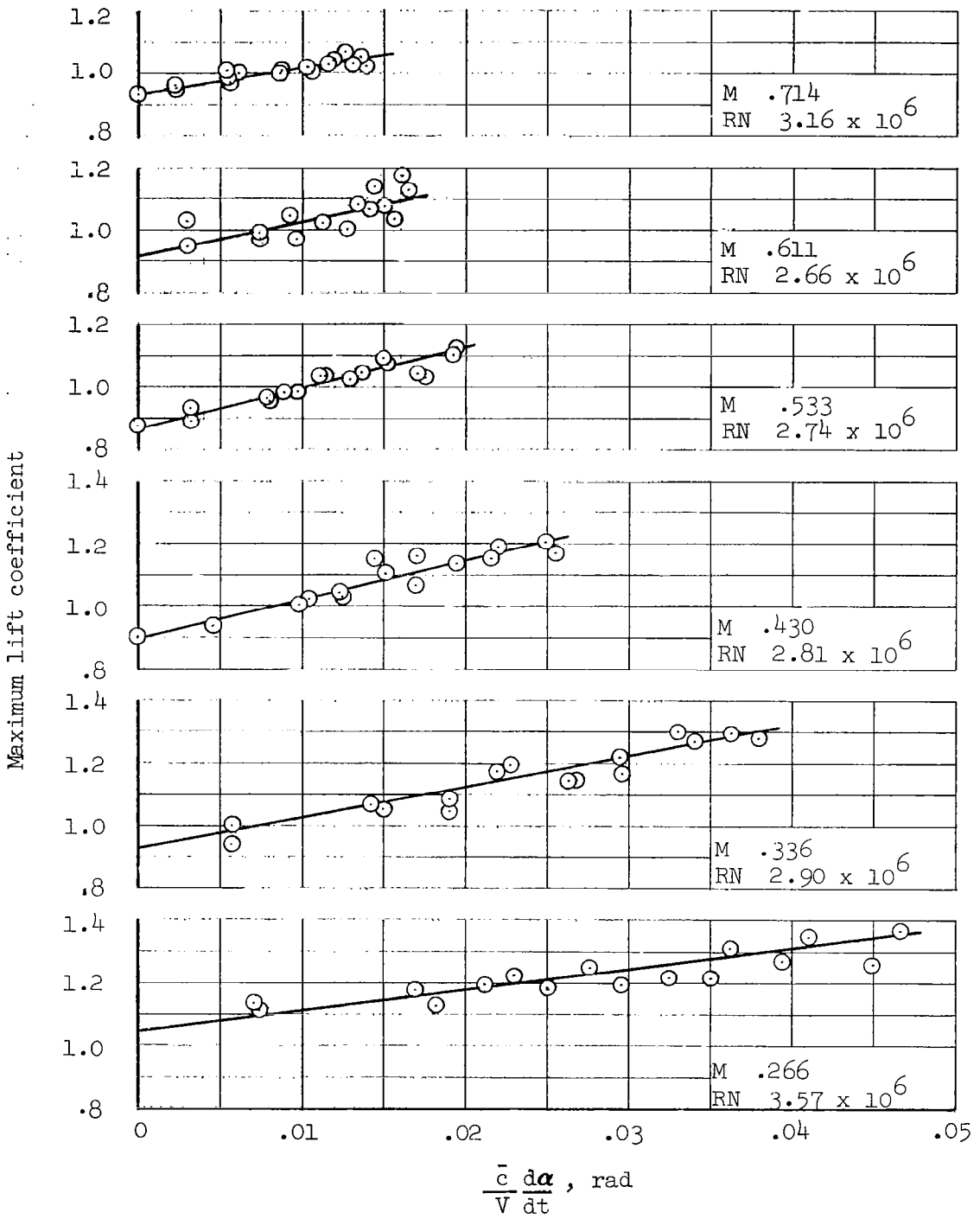

Figure 12 -- Effect of Angle-of-attack Rate on the Maximum Lift Coefficient of Wind Tunnel Wing W-4

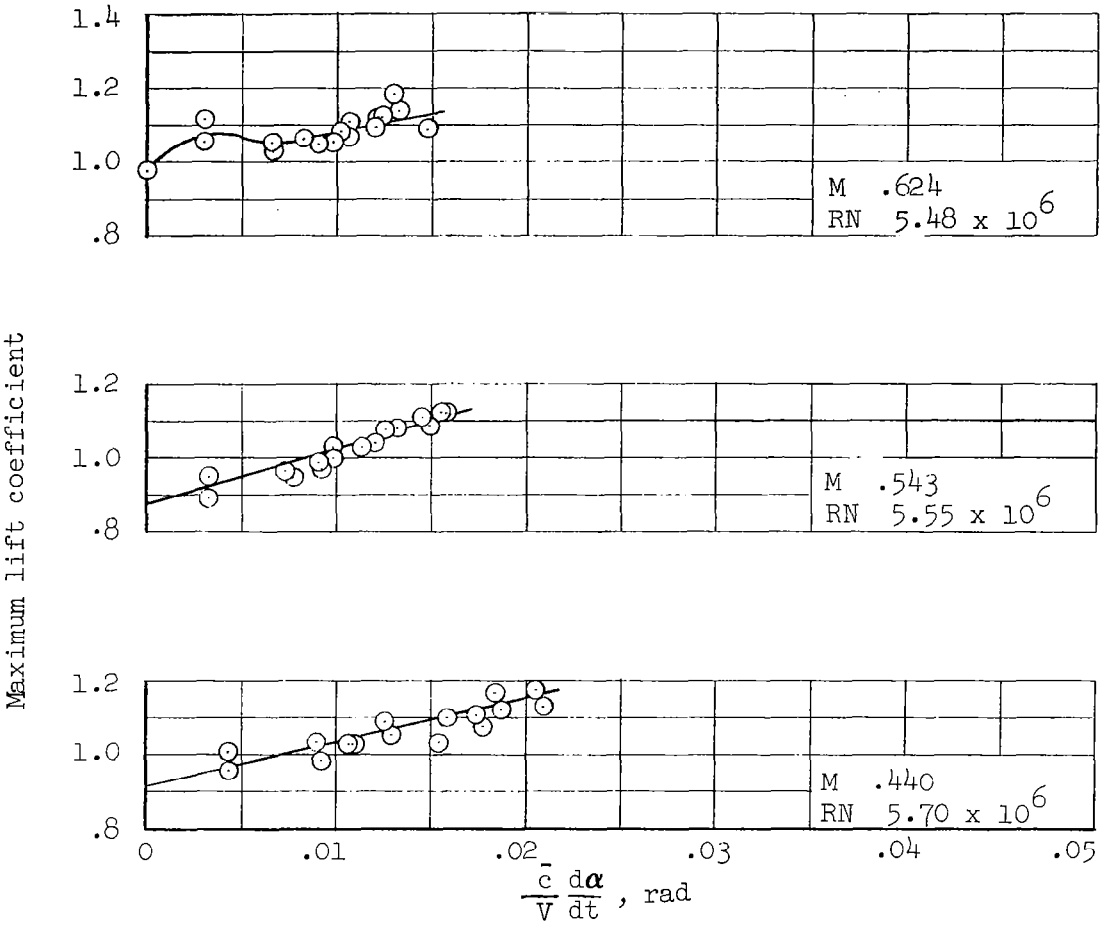

Figure 12 -- Concluded.

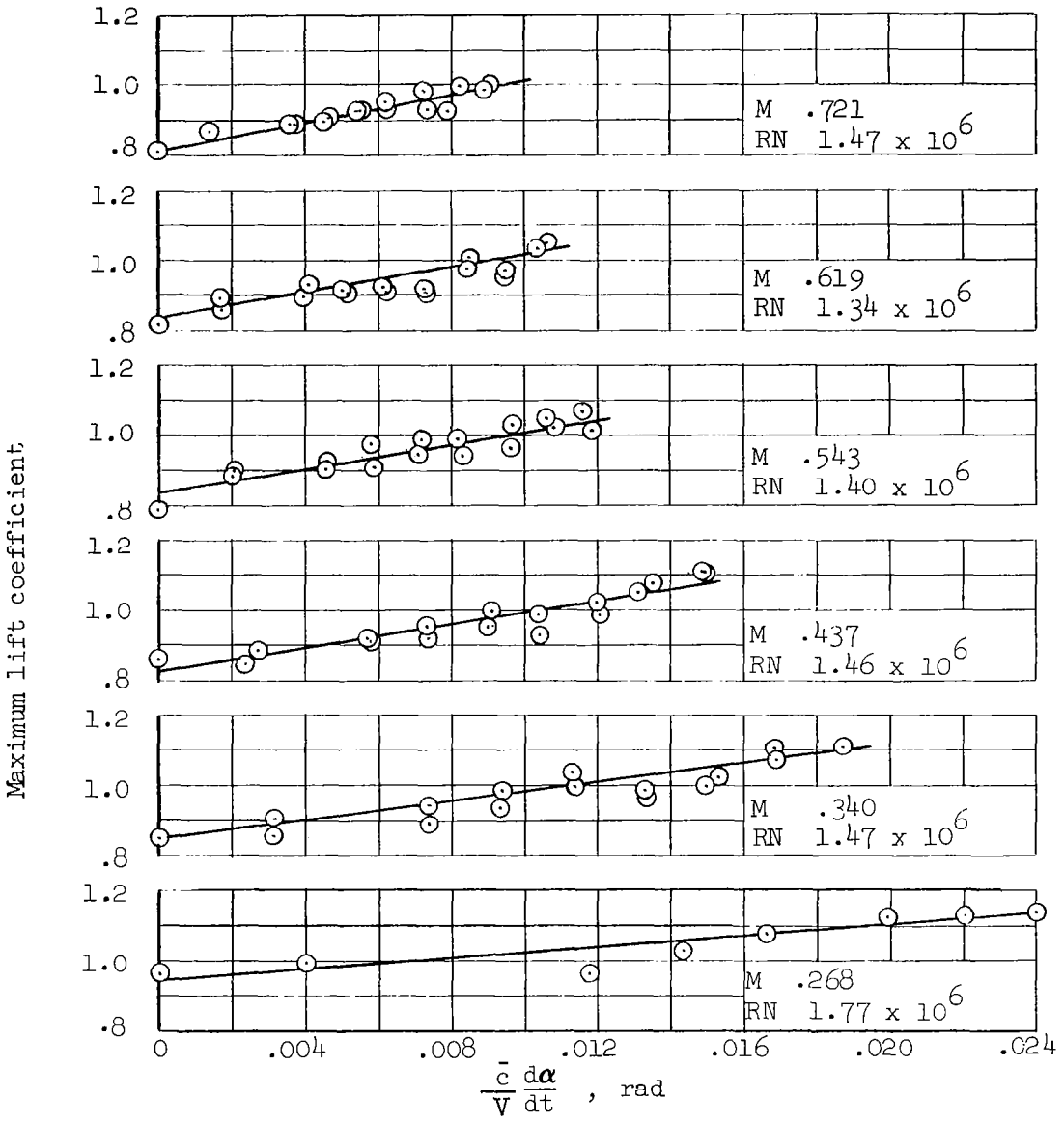

Figure 13 -- Effect of Angle-of-attack Rate on the Maximum Lift Coefficient of Wind Tunnel Wing W-5

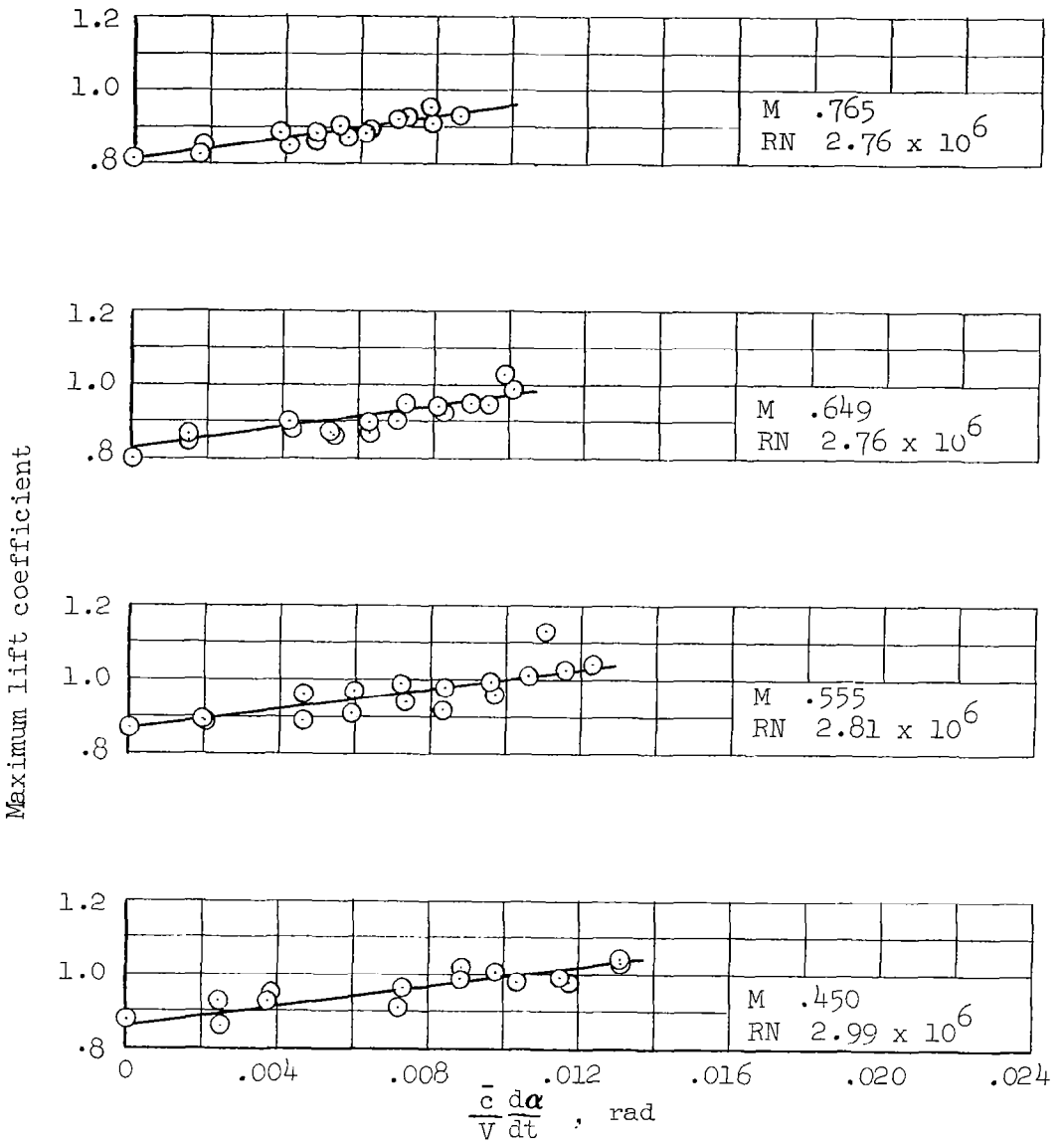

Figure 13 -- Concluded.

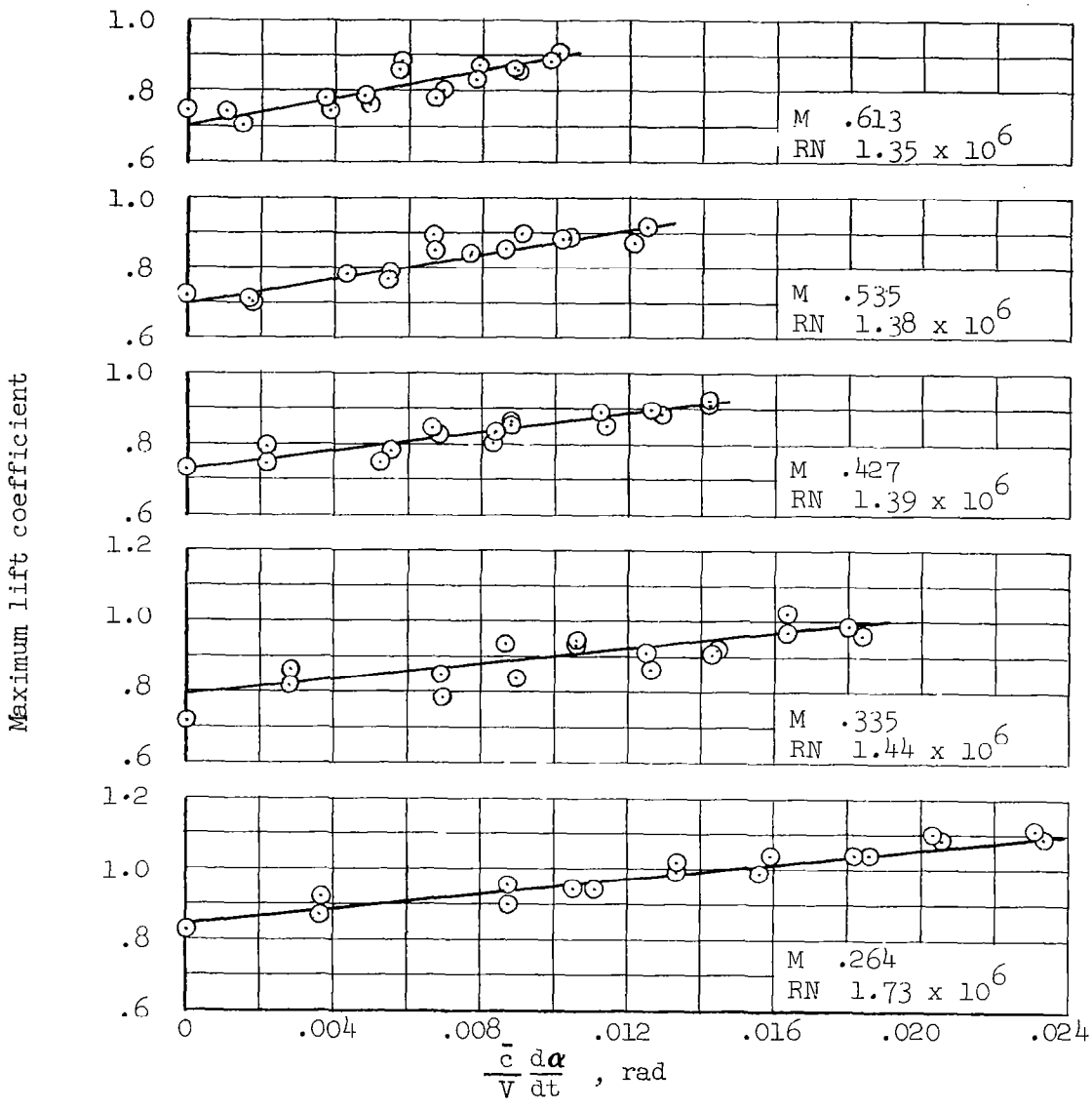

Figure 14 -- Effect of Angle-of-attack Rate on the Maximum Lift Coefficient of Wind Tunnel Wing W-6

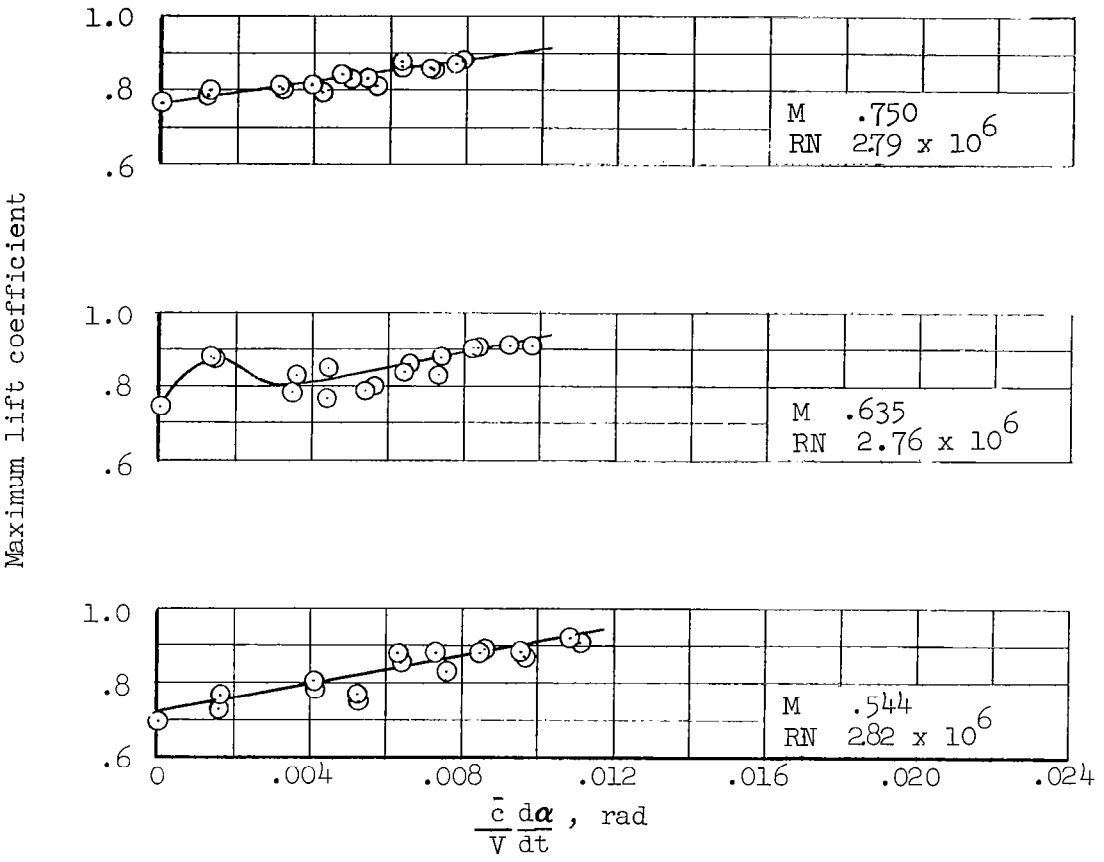

Figure 14 -- Concluded.

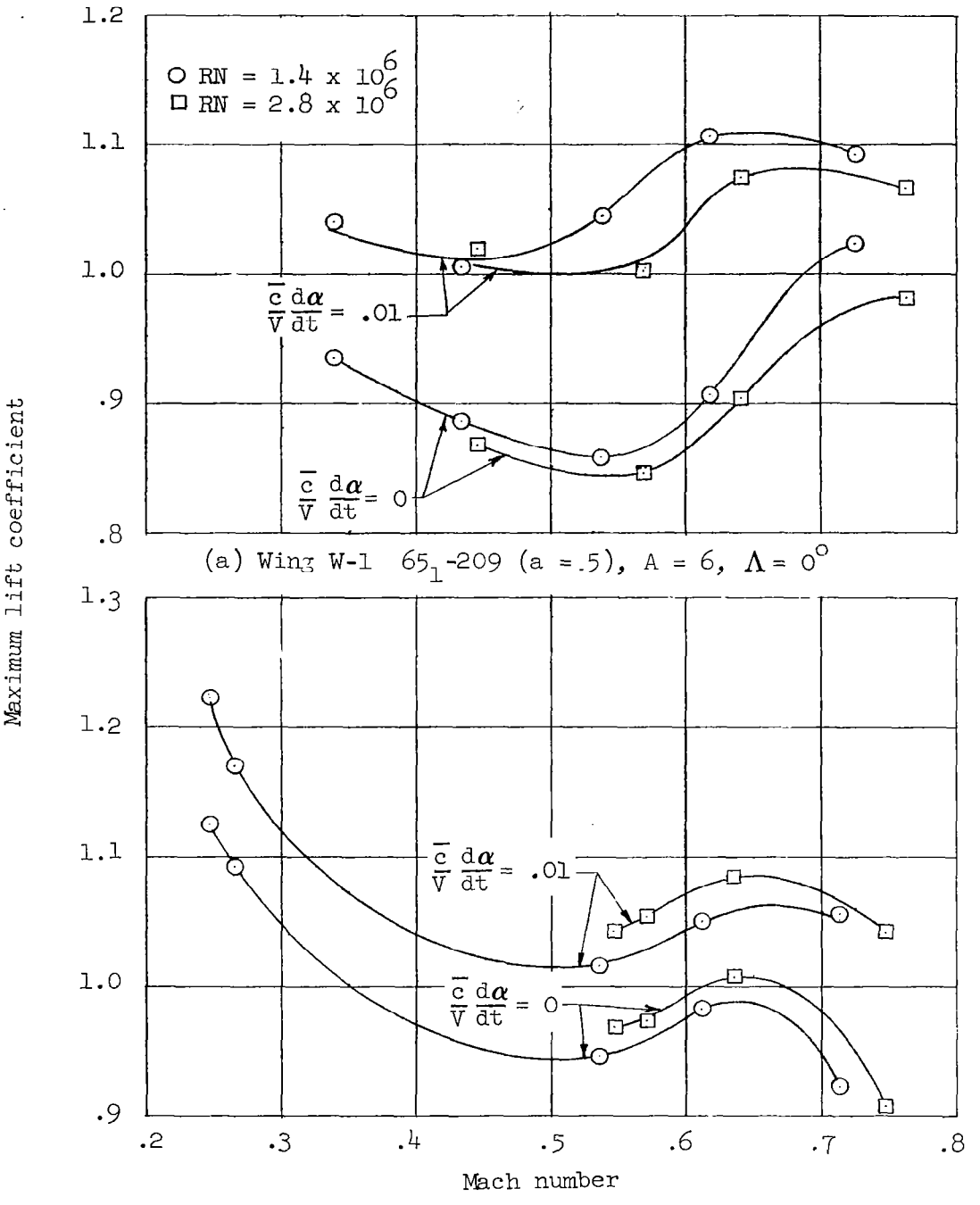

Figure 15 -- Reynolds Number Effect on Maximum Lift Coefficient for Six Wind Tunnel Model Wings.

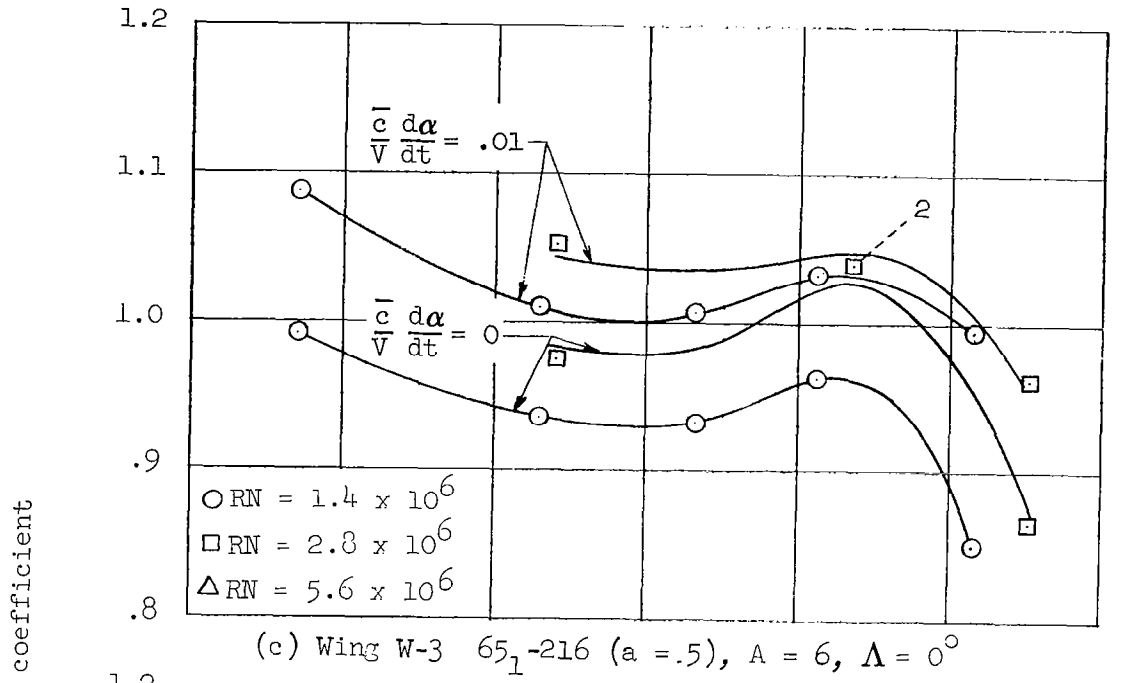

(c) Wing W-3 65_1-216 (a = .5), A = 6, $\Lambda = 0^\circ$

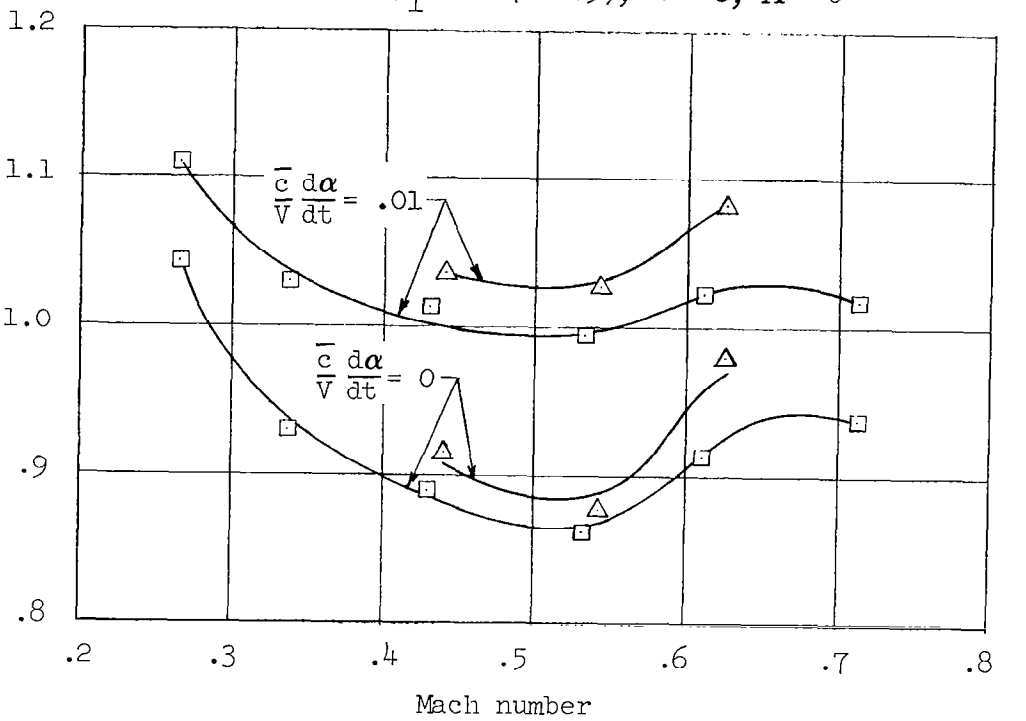

Maximum lift coefficient

(d) Wing W-4 65_1-213 (a = .5), A = 3, $\Lambda = 0^\circ$

Figure 15 -- Continued

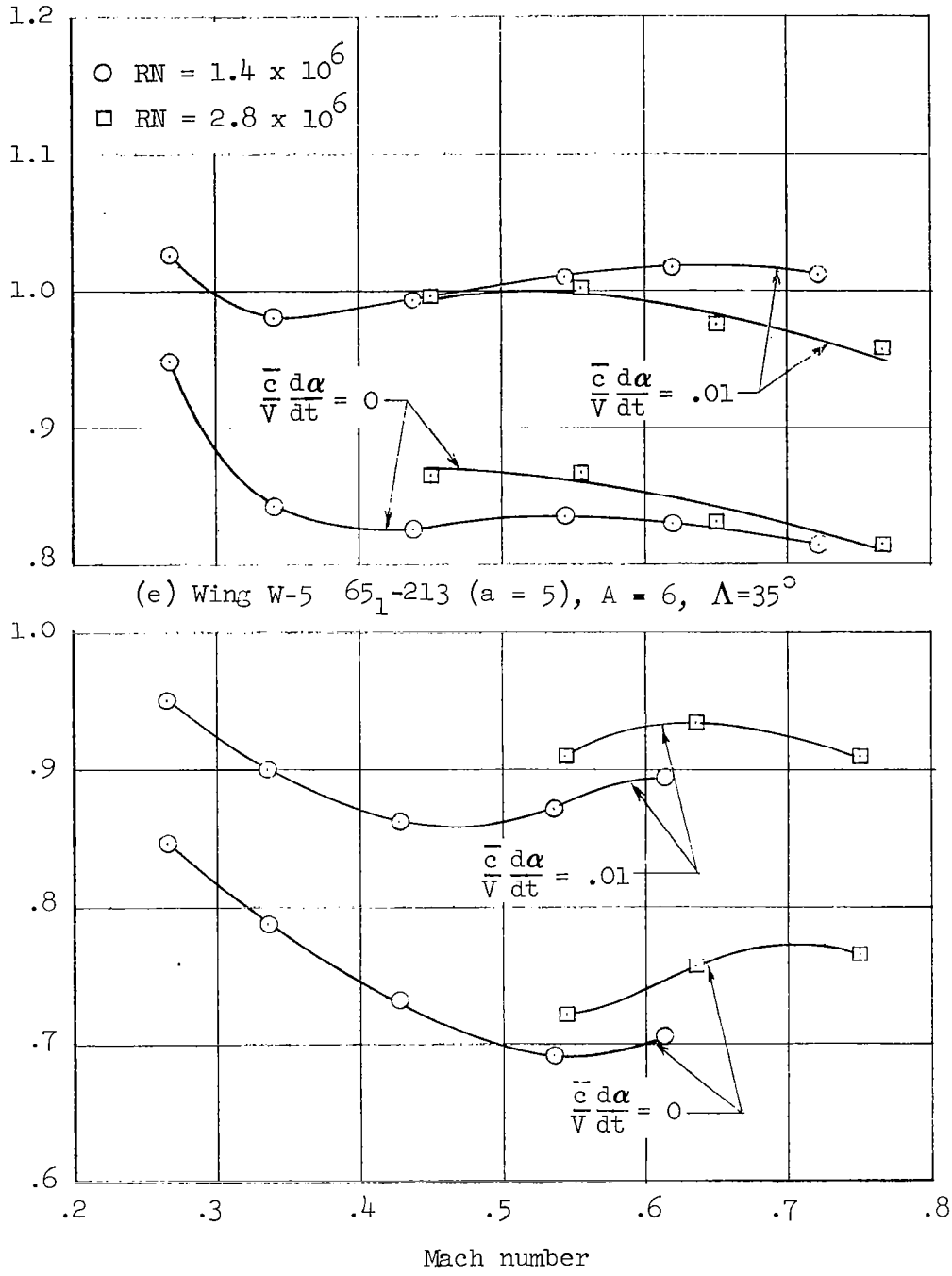

(e) Wing W-5 65_1-213 (a = 5), A = 6, Λ=35°

(f) Wing W-6 65_1-013, A =6, Λ = 0°

Figure 15 -- Concluded

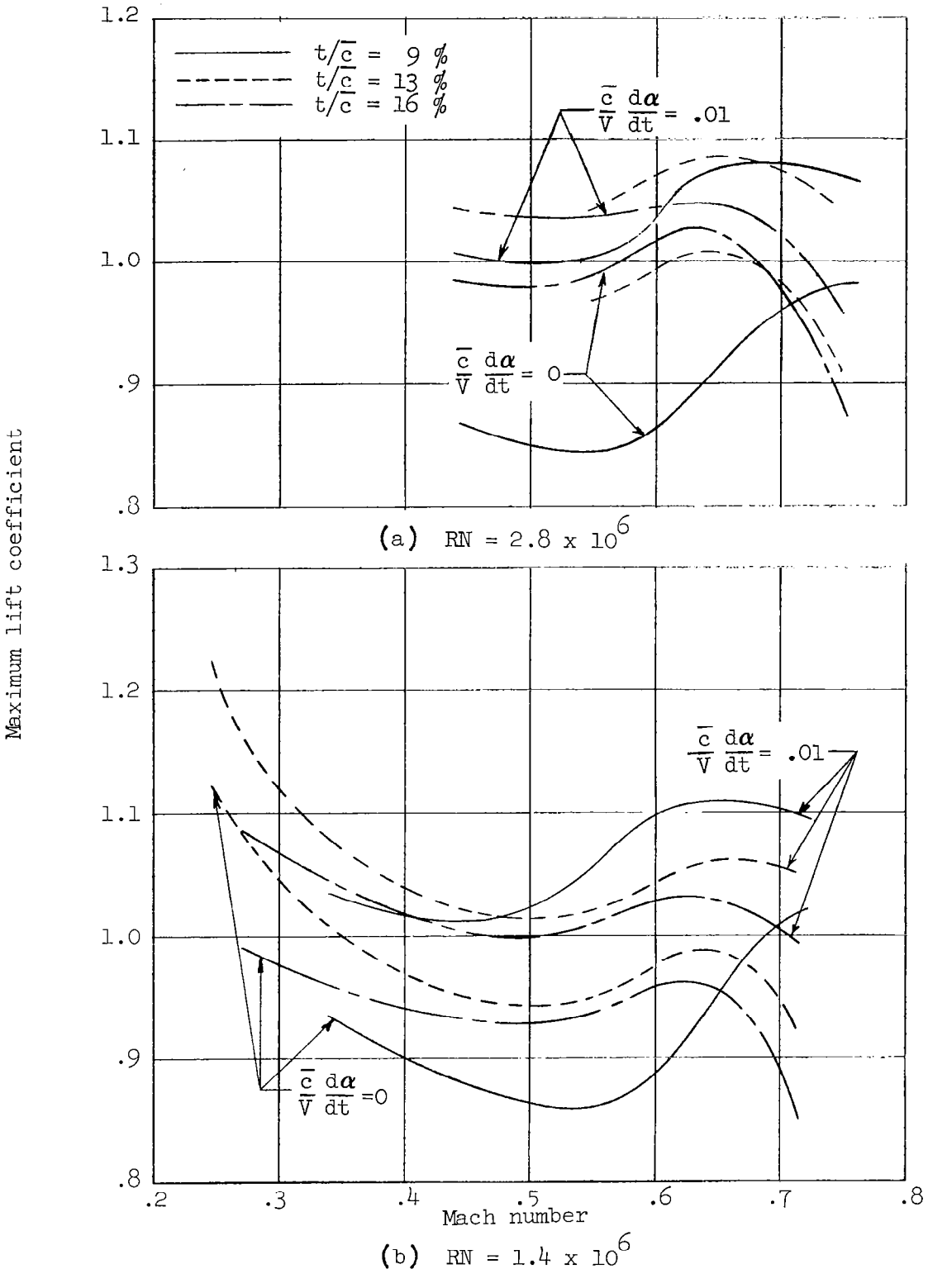

Figure 16 -- Effect of Thickness on Maximum Lift Coefficient

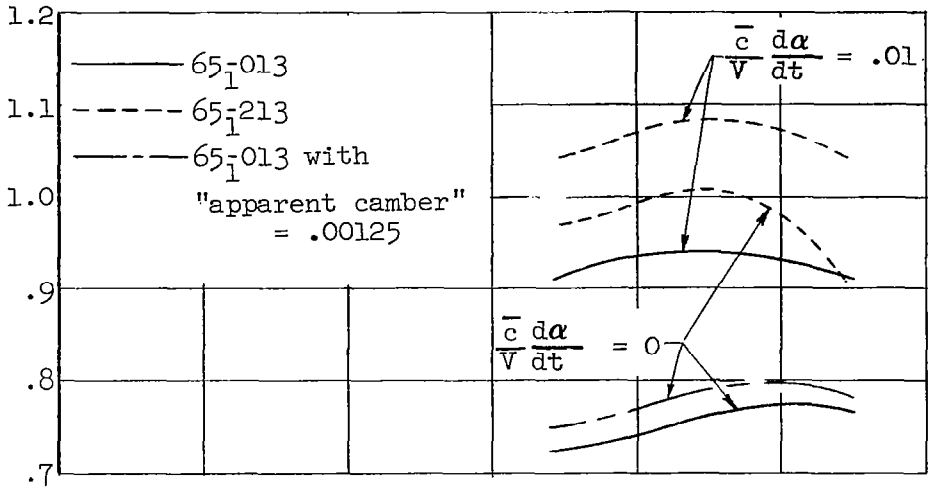

(a) RN = 2.8 x 10^6

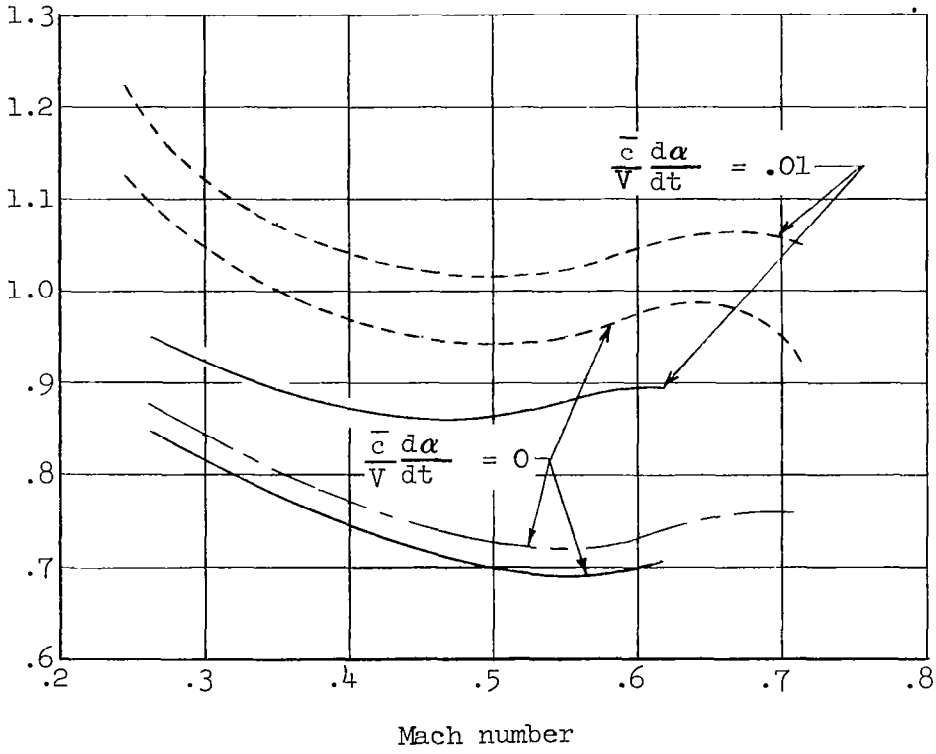

(b) RN = 1.4 x 10^6

Maximum lift coefficient

Figure 17 -- Effect of Camber on Maximum Lift Coefficient

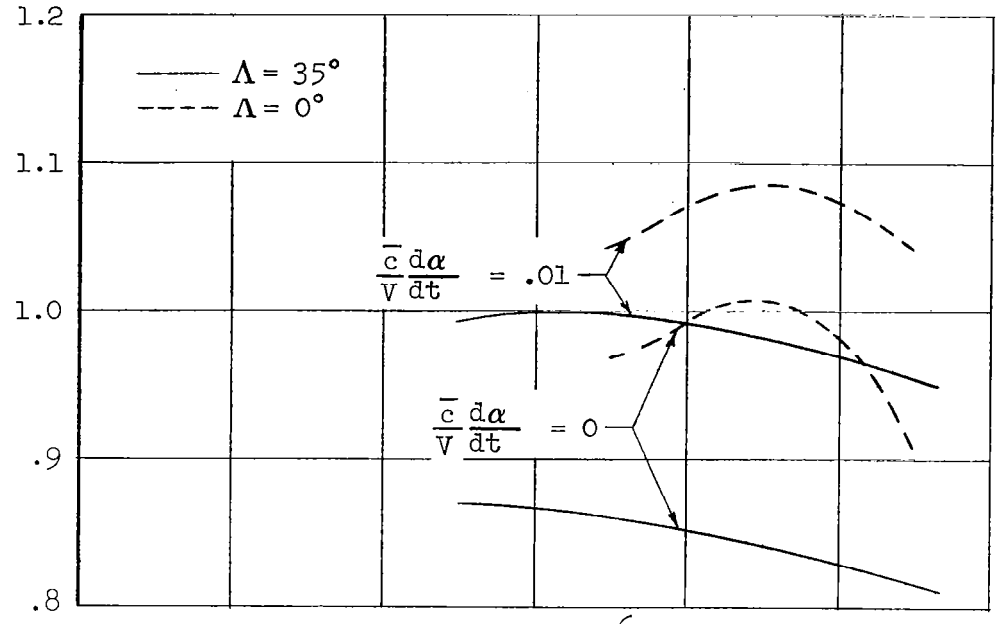

(a) RN = 2.8 x 10^6

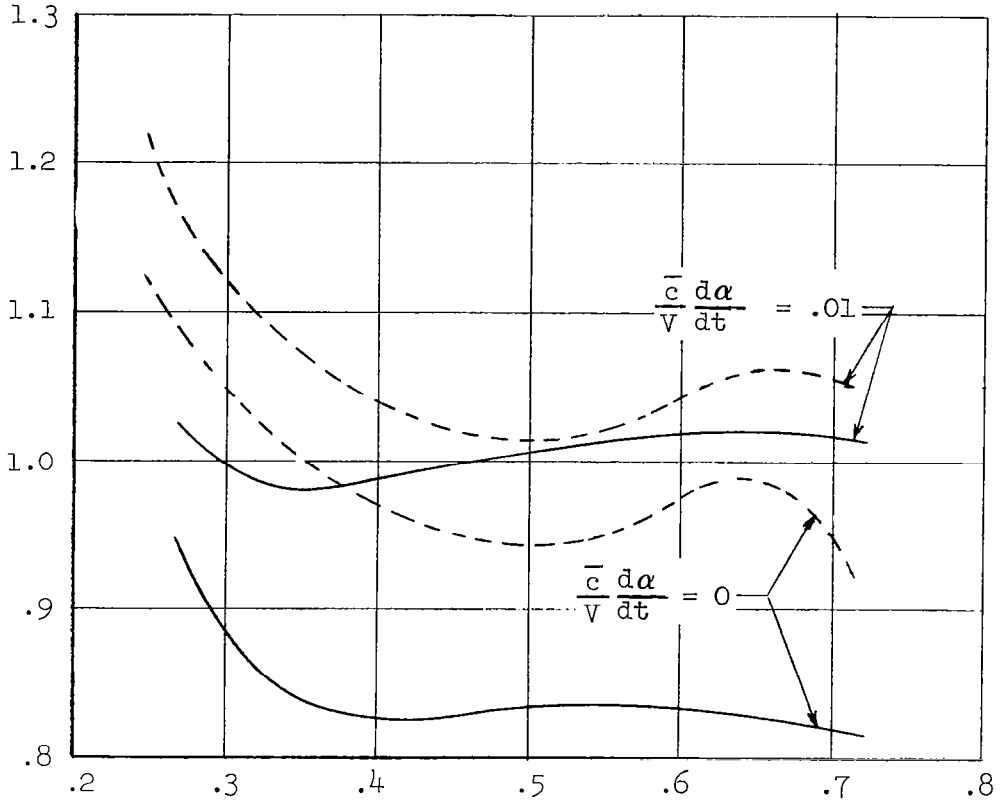

Maximum lift coefficient

(b) RN = 1.4 x 10^6

Figure 18 -- Effect of Sweep on Maximum Lift Coefficient

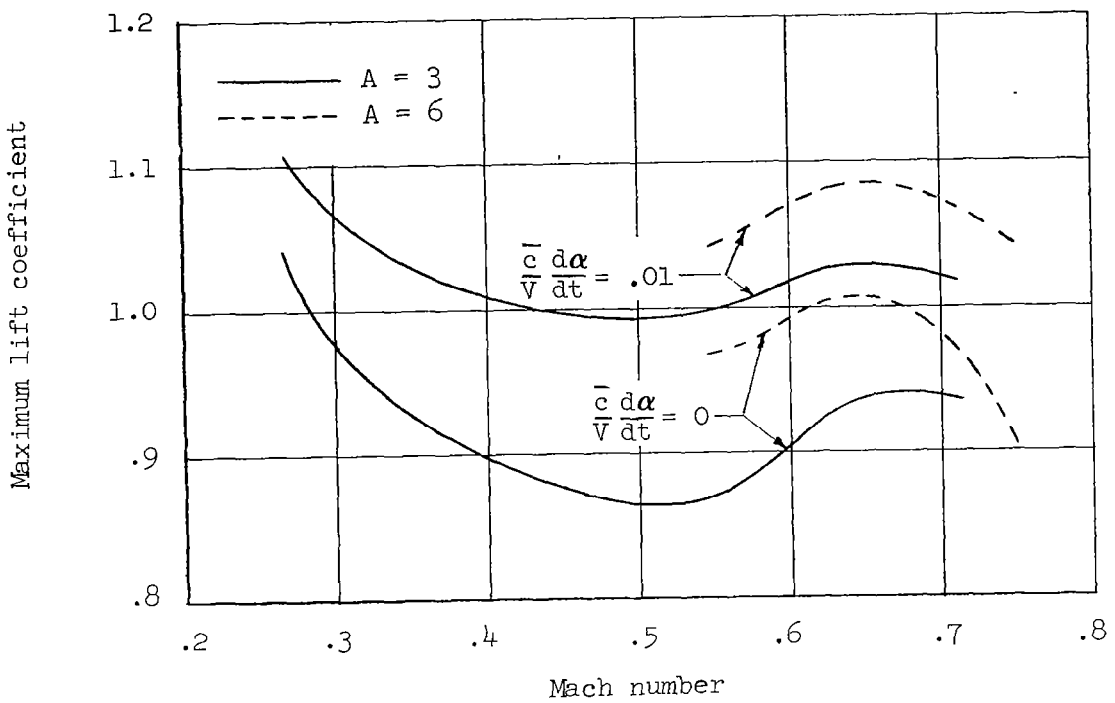

$RN = 2.8 \times 10^6$

Figure 19 -- Effect of Aspect Ratio on Maximum Lift Coefficient

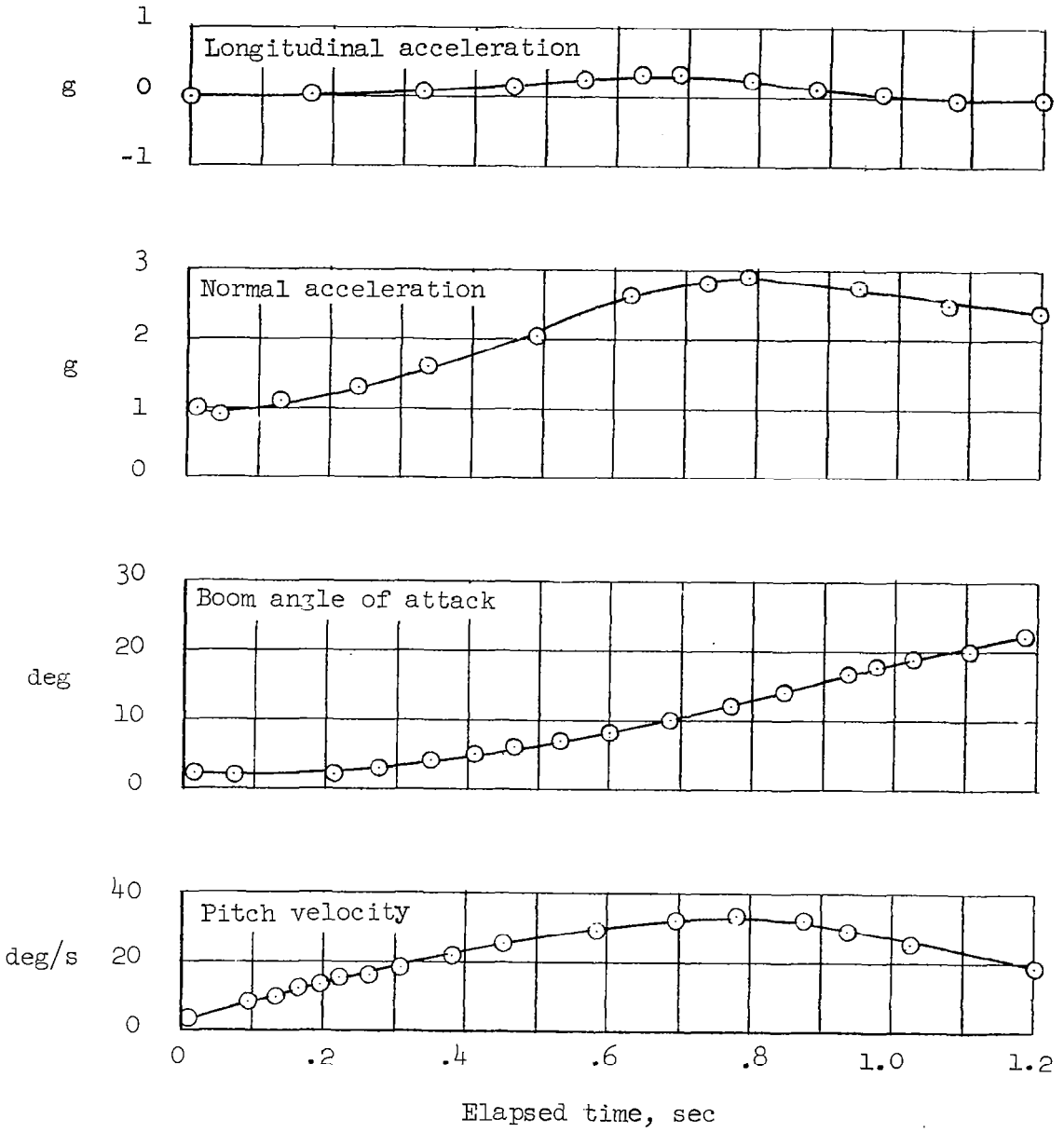

(a) Oscillograph Data

Figure 20 -- Example of Flight Test Data

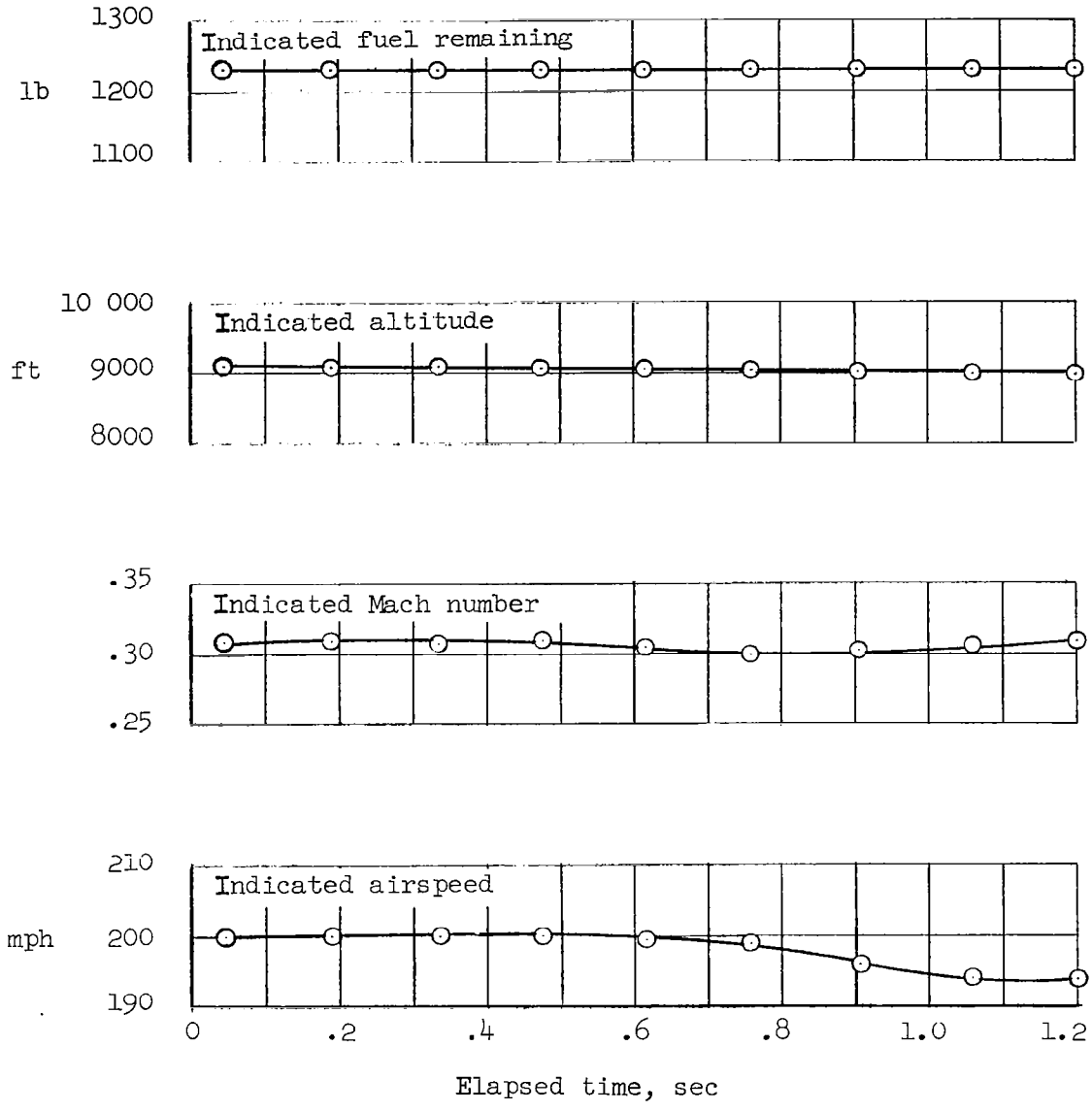

(b) Automatic Observer Data

Figure 20 -- Concluded.

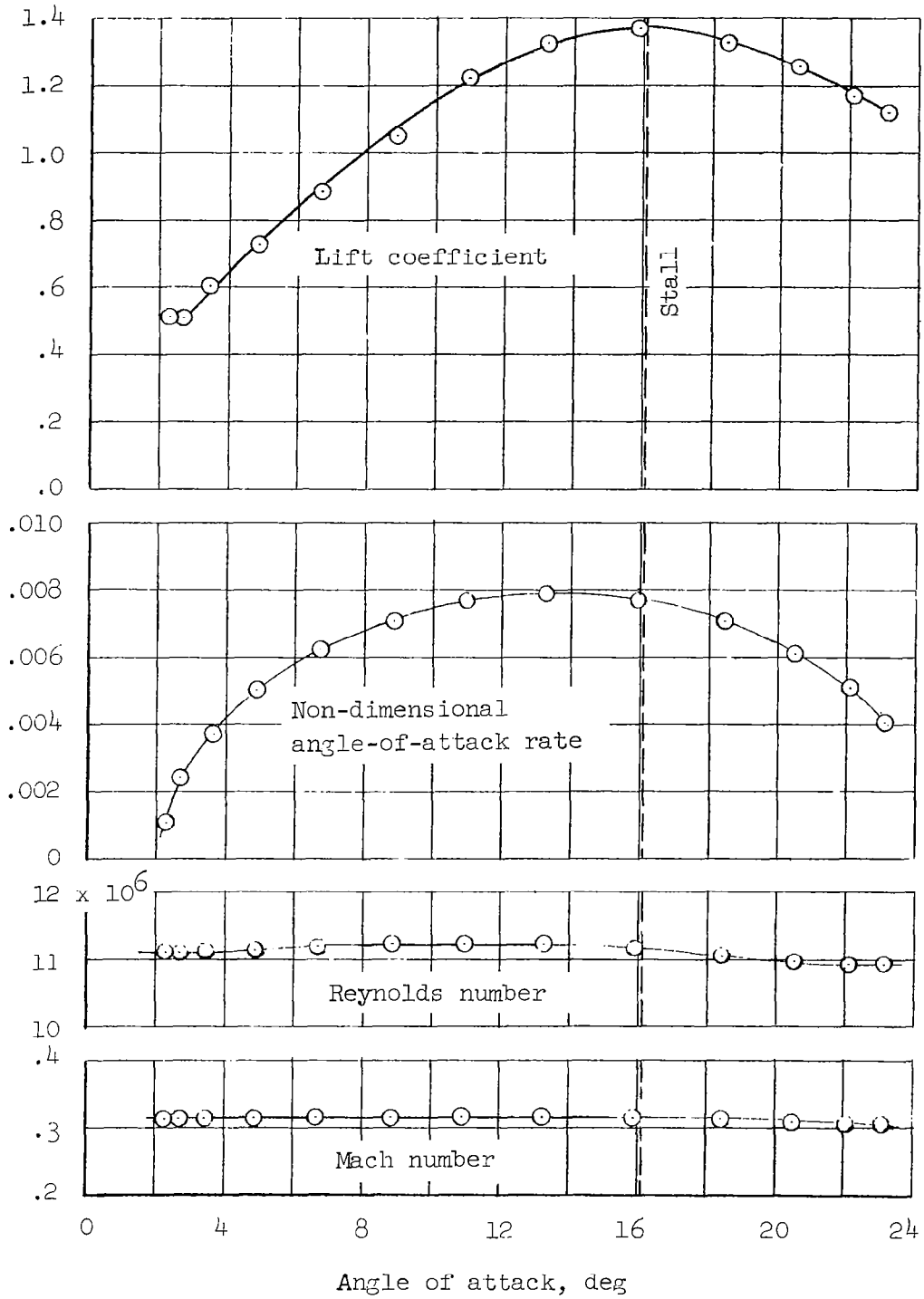

Figure 21 -- Example of Processed Flight Test Data

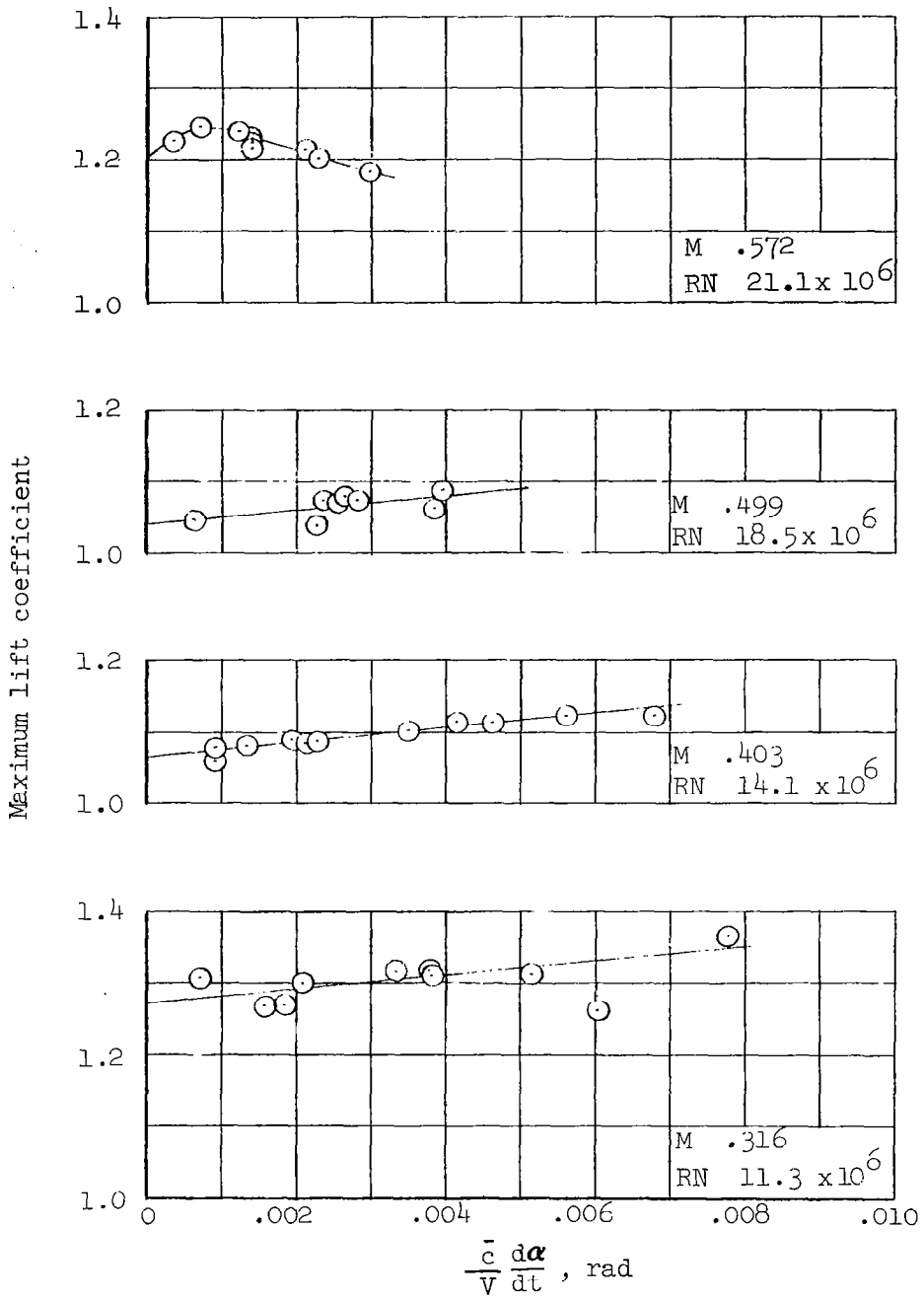

(a) Test Altitude = 10 000 ft

Figure 22 -- Effect of Angle-of-attack Rate on the Maximum Lift Coefficient of T-1A Airplane

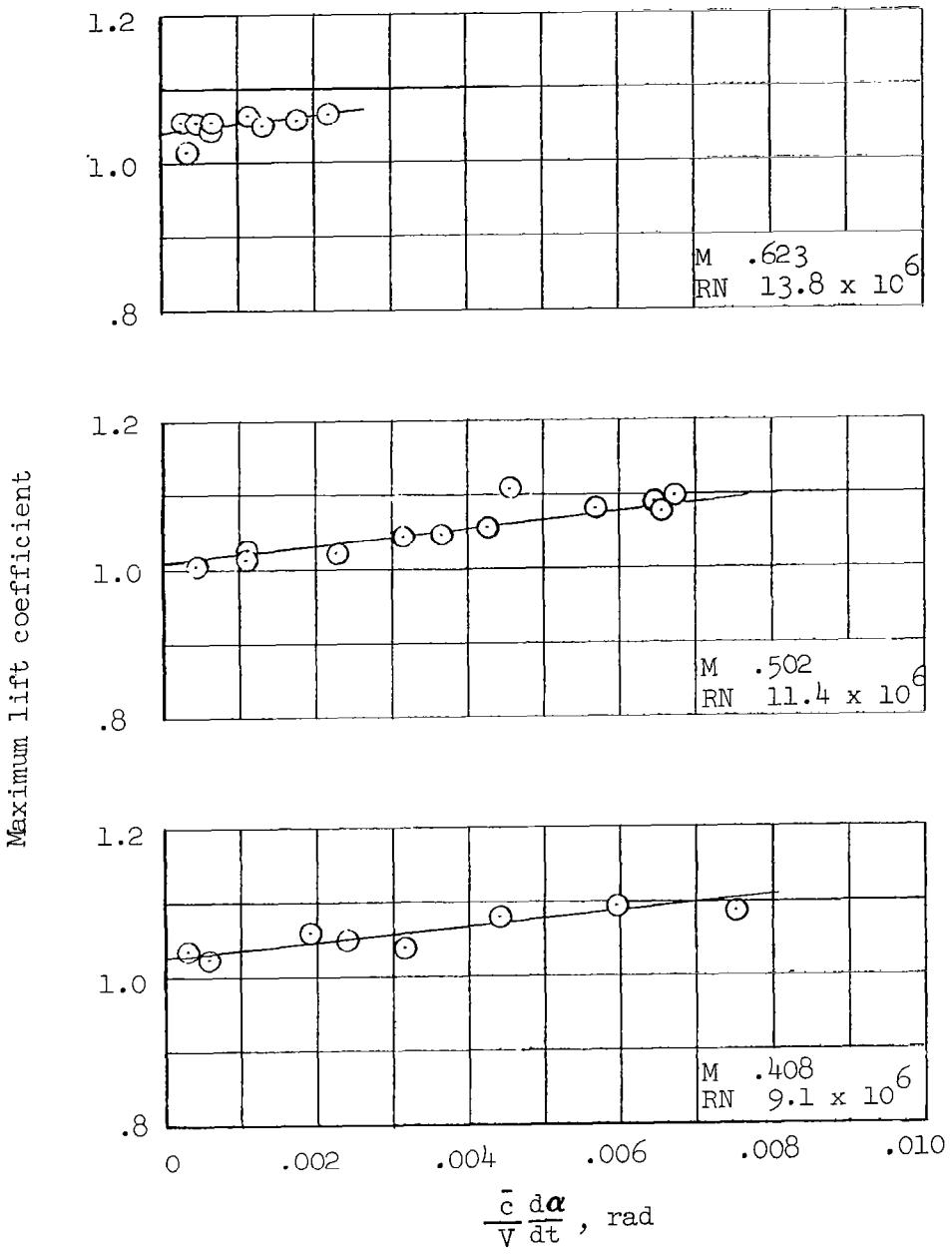

(b) Test Altitude = 25 000 ft

Figure 22 -- Continued.

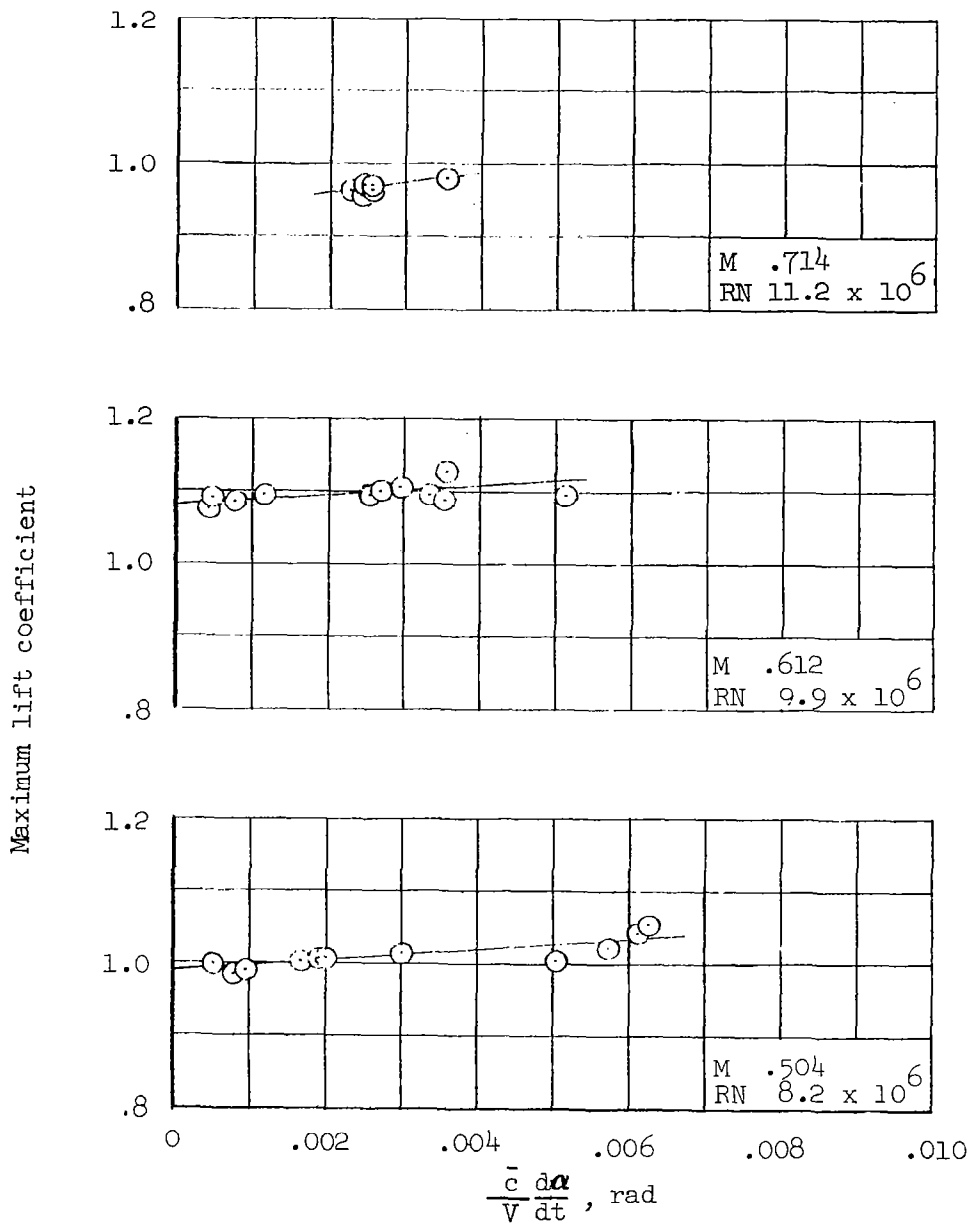

(c) Test Altitude = 35 000 ft

Figure 22 -- Concluded.

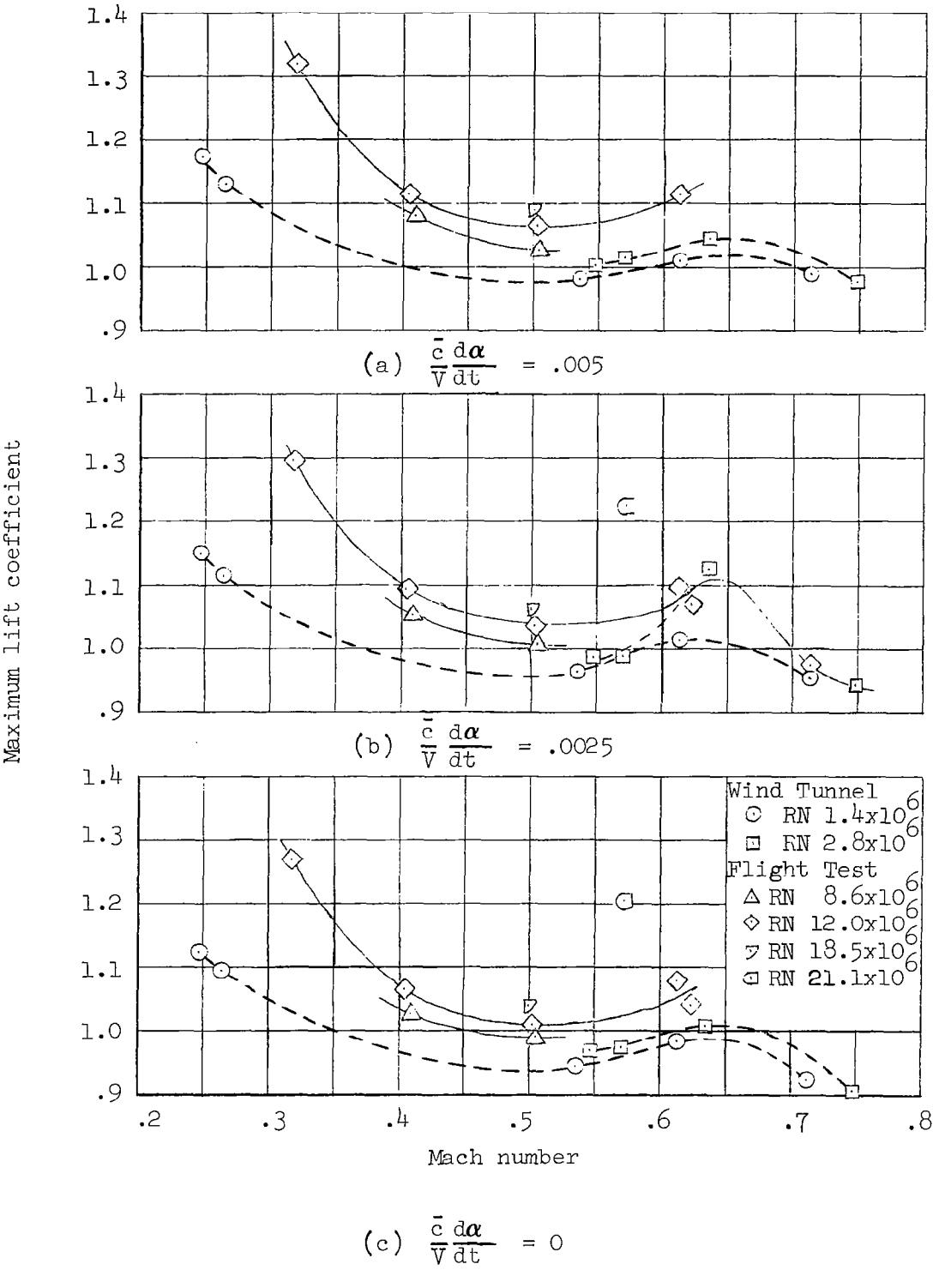

Figure 23 -- Effect of Reynolds Number and Angle-of-attack Rate on Maximum Lift Coefficient of T-1A Airplane Compared with Wind Tunnel Wing W-2

REFERENCES

1. Harper, Paul W.; and Flanigan, Roy E.: The Effect of Rate of Change of Angle-of-Attack on the Maximum Lift of a Small Model. NACA TN 2061, 1950.
2. Gadeberg, Burnett L.: The Effect of Rate of Change of Angle of Attack on the Maximum Lift Coefficient of a Pursuit Airplane. NACA TN 2525, 1951.
3. Spreiter, John R.; Galster, George M.; Blair, William K.: Effect of Mach and Reynolds Numbers on the Maximum Lift Coefficient Obtainable in Gradual and Abrupt Stalls of a Pursuit Airplane Equipped with a Low-Drag Wing. NACA MR A5G06, 1945.
4. Shapiro, Ascher H.: The Dynamics and Thermodynamics of Compressible Fluid Flow. The Ronald Press Co., 1954.
5. McFadden, Norman N.; Holden, George R.; Ratcliff, Jack W.: Instrumentation and Calibration Techniques for Flight Calibration of Angle-of-Attack Systems on Aircraft. NACA RM A52I23, 1952.
6. Garner, H. C.: Note on Aerodynamic Camber. R. & M. 2820 British A.R.C., 1953.
7. Summers, James L.; Treon, Stuart L.: The Effects of Amount and Type of Camber on the Variations with Mach Number of the Aerodynamic Characteristic of a 10 Percent-Thick NACA 64A Series Airfoil Section. NACA TN 2096, 1950.